Measurement of two-particle correlations with respect to second- and third-order event planes in Au + Au collisions at $\sqrt{s_{NN}} = 200$ GeV

A. Adare,[13] S. Afanasiev,[32] C. Aidala,[46,47] N. N. Ajitanand,[67,*] Y. Akiba,[61,62,†] H. Al-Bataineh,[55] J. Alexander,[67] M. Alfred,[25] K. Aoki,[34,37,61] Y. Aramaki,[12] E. T. Atomssa,[38] R. Averbeck,[68] T. C. Awes,[57] B. Azmoun,[7] V. Babintsev,[26] A. Bagoly,[18] M. Bai,[6] G. Baksay,[21] L. Baksay,[21] K. N. Barish,[8] B. Bassalleck,[54] A. T. Basye,[1] S. Bathe,[5,8,62] V. Baublis,[60] C. Baumann,[48] A. Bazilevsky,[7] S. Belikov,[7,*] R. Belmont,[13,73] R. Bennett,[68] A. Berdnikov,[64] Y. Berdnikov,[64] A. A. Bickley,[13] M. Boer,[41] J. S. Bok,[55,77] K. Boyle,[62,68] M. L. Brooks,[41] J. Bryslawskyj,[8] H. Buesching,[7] V. Bumazhnov,[26] G. Bunce,[7,62] S. Butsyk,[41] C. M. Camacho,[41] S. Campbell,[14,68] V. Canoa Roman,[68] C.-H. Chen,[62,68] C. Y. Chi,[14] M. Chiu,[7] I. J. Choi,[27,77] R. K. Choudhury,[4] P. Christiansen,[43] T. Chujo,[72] P. Chung,[67] O. Chvala,[8] V. Cianciolo,[57] Z. Citron,[68,75] B. A. Cole,[14] M. Connors,[23,62,68] P. Constantin,[41] M. Csanád,[18] T. Csörgő,[19,76] T. Dahms,[68] S. Dairaku,[37,61] I. Danchev,[73] T. W. Danley,[56] K. Das,[22] A. Datta,[46] G. David,[7,68] K. Dehmelt,[21,68] A. Denisov,[26] A. Deshpande,[62,68] E. J. Desmond,[7] O. Dietzsch,[65] A. Dion,[68] J. H. Do,[77] M. Donadelli,[65] O. Drapier,[38] A. Drees,[68] K. A. Drees,[6] J. M. Durham,[41,68] A. Durum,[26] D. Dutta,[4] S. Edwards,[22] Y. V. Efremenko,[57] F. Ellinghaus,[13] T. Engelmore,[14] A. Enokizono,[40,61,63] H. En'yo,[61,62] S. Esumi,[72] B. Fadem,[49] W. Fan,[68] N. Feege,[68] D. E. Fields,[54] M. Finger,[9] M. Finger, Jr.,[9] F. Fleuret,[38] S. L. Fokin,[36] Z. Fraenkel,[75,*] J. E. Frantz,[56,68] A. Franz,[7] A. D. Frawley,[22] K. Fujiwara,[61] Y. Fukao,[61] T. Fusayasu,[51] P. Gallus,[15] P. Garg,[3,68] I. Garishvili,[40,70] H. Ge,[68] A. Glenn,[13,40] H. Gong,[68] M. Gonin,[38] Y. Goto,[61,62] R. Granier de Cassagnac,[38] N. Grau,[2,14] S. V. Greene,[73] M. Grosse Perdekamp,[27,62] T. Gunji,[12] H.-Å. Gustafsson,[43,*] T. Hachiya,[24,52,62] J. S. Haggerty,[7] K. I. Hahn,[20] H. Hamagaki,[12] J. Hamblen,[70] R. Han,[59] J. Hanks,[14,68] E. P. Hartouni,[40] S. Hasegawa,[31] T. O. S. Haseler,[23] E. Haslum,[43] R. Hayano,[12] X. He,[23] M. Heffner,[40] T. K. Hemmick,[68] T. Hester,[8] J. C. Hill,[30] K. Hill,[13] A. Hodges,[23] M. Hohlmann,[21] W. Holzmann,[14] K. Homma,[24] B. Hong,[35] T. Horaguchi,[24] D. Hornback,[70] N. Hotvedt,[30] J. Huang,[7] S. Huang,[73] T. Ichihara,[61,62] R. Ichimiya,[61] J. Ide,[49] Y. Ikeda,[72] K. Imai,[31,37,61] M. Inaba,[72] D. Isenhower,[1] M. Ishihara,[61] T. Isobe,[12,61] M. Issah,[73] A. Isupov,[32] D. Ivanishchev,[60] B. V. Jacak,[68] Z. Ji,[68] J. Jia,[7,67] J. Jin,[14] B. M. Johnson,[7,23] K. S. Joo,[50] D. Jouan,[58] D. S. Jumper,[1,27] F. Kajihara,[12] S. Kametani,[61] N. Kamihara,[62] J. Kamin,[68] J. H. Kang,[77] J. Kapustinsky,[41] K. Karatsu,[37,61] D. Kawall,[46,62] M. Kawashima,[61,63] A. V. Kazantsev,[36] T. Kempel,[30] V. Khachatryan,[68] A. Khanzadeev,[60] K. M. Kijima,[24] B. I. Kim,[35] D. H. Kim,[50] D. J. Kim,[33] E. Kim,[66] E.-J. Kim,[10] M. Kim,[66] S. H. Kim,[77] Y.-J. Kim,[27] D. Kincses,[18] E. Kinney,[13] K. Kiriluk,[13] Á. Kiss,[18] E. Kistenev,[7] L. Kochenda,[60] B. Komkov,[60] M. Konno,[72] J. Koster,[27] D. Kotchetkov,[54,56] D. Kotov,[60,64] A. Kozlov,[75] A. Král,[15] A. Kravitz,[14] G. J. Kunde,[41] B. Kurgyis,[18] K. Kurita,[61,63] M. Kurosawa,[61,62] Y. Kwon,[77] G. S. Kyle,[55] R. Lacey,[67] Y. S. Lai,[14] J. G. Lajoie,[30] A. Lebedev,[30] D. M. Lee,[41] J. Lee,[20,69] K. Lee,[66] K. B. Lee,[35] K. S. Lee,[35] S. H. Lee,[30] M. J. Leitch,[41] M. A. L. Leite,[65] E. Leitner,[73] B. Lenzi,[65] Y. H. Leung,[68] N. A. Lewis,[47] X. Li,[11] X. Li,[41] P. Liebing,[62] S. H. Lim,[41,77] L. A. Linden Levy,[13] T. Liška,[15] A. Litvinenko,[32] H. Liu,[41,55] M. X. Liu,[41] S. Lökös,[18,19] B. Love,[73] R. Luechtenborg,[48] D. Lynch,[7] C. F. Maguire,[73] T. Majoros,[17] Y. I. Makdisi,[6] A. Malakhov,[32] M. D. Malik,[54] V. I. Manko,[36] E. Mannel,[7,14] Y. Mao,[59,61] H. Masui,[72] F. Matathias,[14] M. McCumber,[41,68] P. L. McGaughey,[41] D. McGlinchey,[13,41] N. Means,[68] B. Meredith,[27] Y. Miake,[72] A. C. Mignerey,[45] D. E. Mihalik,[68] P. Mikeš,[9,29] K. Miki,[61,72] A. Milov,[7,75] M. Mishra,[3] J. T. Mitchell,[7] G. Mitsuka,[34,62] S. Mizuno,[61,72] A. K. Mohanty,[4] T. Moon,[77] Y. Morino,[12] A. Morreale,[8] D. P. Morrison,[7] S. I. Morrow,[73] T. V. Moukhanova,[36] J. Murata,[61,63] S. Nagamiya,[34,61] K. Nagashima,[24] J. L. Nagle,[13] M. Naglis,[75] M. I. Nagy,[18] I. Nakagawa,[61,62] Y. Nakamiya,[24] T. Nakamura,[34] K. Nakano,[61,71] C. Nattrass,[70] J. Newby,[40] M. Nguyen,[68] T. Niida,[72] R. Nouicer,[7,62] T. Novák,[19] N. Novitzky,[68] A. S. Nyanin,[36] E. O'Brien,[7] S. X. Oda,[12] C. A. Ogilvie,[30] M. Oka,[72] K. Okada,[62] Y. Onuki,[61] J. D. Orjuela Koop,[13] J. D. Osborn,[47] A. Oskarsson,[43] M. Ouchida,[24,61] K. Ozawa,[12,34,72] R. Pak,[7] V. Pantuev,[28,68] V. Papavassiliou,[55] I. H. Park,[20,69] J. Park,[66] S. Park,[61,66,68] S. K. Park,[35] W. J. Park,[35] S. F. Pate,[55] M. Patel,[30] H. Pei,[30] J.-C. Peng,[27] W. Peng,[73] H. Pereira,[16] D. V. Perepelitsa,[13] V. Peresedov,[32] D. Yu. Peressounko,[36] C. E. PerezLara,[68] C. Pinkenburg,[7] R. P. Pisani,[7] M. Proissl,[68] M. L. Purschke,[7] A. K. Purwar,[41] H. Qu,[23] P. V. Radzevich,[64] J. Rak,[33] A. Rakotozafindrabe,[38] I. Ravinovich,[75] K. F. Read,[57,70] K. Reygers,[48] V. Riabov,[53,60] Y. Riabov,[60,64] E. Richardson,[45] D. Richford,[5] T. Rinn,[30] D. Roach,[73] G. Roche,[42,*] S. D. Rolnick,[8] M. Rosati,[30] C. A. Rosen,[13] S. S. E. Rosendahl,[43] P. Rosnet,[42] Z. Rowan,[5] P. Rukoyatkin,[32] J. Runchey,[30] P. Ružička,[29] B. Sahlmueller,[48,68] N. Saito,[34] T. Sakaguchi,[7] K. Sakashita,[61,71] H. Sako,[31] V. Samsonov,[53,60] S. Sano,[12,74] M. Sarsour,[23] S. Sato,[31,34] T. Sato,[72] S. Sawada,[34] B. K. Schmoll,[70] K. Sedgwick,[8] J. Seele,[13] R. Seidl,[27,61,62] A. Yu. Semenov,[30] R. Seto,[8] D. Sharma,[68,75] I. Shein,[26] T.-A. Shibata,[61,71] K. Shigaki,[24] M. Shimomura,[30,52,72] K. Shoji,[37,61] P. Shukla,[4] A. Sickles,[7,27] C. L. Silva,[41,65] D. Silvermyr,[43,57] C. Silvestre,[16] K. S. Sim,[35] B. K. Singh,[3] C. P. Singh,[3] V. Singh,[3] M. J. Skoby,[47] M. Slunečka,[9] R. A. Soltz,[40] W. E. Sondheim,[41] S. P. Sorensen,[70] I. V. Sourikova,[7] N. A. Sparks,[1] P. W. Stankus,[57] E. Stenlund,[43] S. P. Stoll,[7] T. Sugitate,[24] A. Sukhanov,[7] Z. Sun,[17] J. Sziklai,[76] E. M. Takagui,[65] A. Taketani,[61,62] R. Tanabe,[72] Y. Tanaka,[51] K. Tanida,[31,37,61,62,66] M. J. Tannenbaum,[7] S. Tarafdar,[3,73] A. Taranenko,[53,67] P. Tarján,[17] H. Themann,[68] T. L. Thomas,[54] R. Tieulent,[44] T. Todoroki,[61,62,72] M. Togawa,[37,61] A. Toia,[68] L. Tomášek,[29] H. Torii,[24] R. S. Towell,[1] I. Tserruya,[75] Y. Tsuchimoto,[24] Y. Ueda,[24] B. Ujvari,[17] C. Vale,[7,30] H. Valle,[73] H. W. van Hecke,[41] E. Vazquez-Zambrano,[14] A. Veicht,[14,27] J. Velkovska,[73] R. Vértesi,[17,76] A. A. Vinogradov,[36] M. Virius,[15] V. Vrba,[15,29] E. Vznuzdaev,[60] X. R. Wang,[55,62] D. Watanabe,[24] K. Watanabe,[72] Y. Watanabe,[61,62] F. Wei,[30,55] R. Wei,[67] J. Wessels,[48] S. N. White,[7] D. Winter,[14] C. P. Wong,[23] J. P. Wood,[1]

C. L. Woody,[7] R. M. Wright,[1] M. Wysocki,[13,57] W. Xie,[62] C. Xu,[55] Q. Xu,[73] Y. L. Yamaguchi,[12,62,68] K. Yamaura,[24] R. Yang,[27] A. Yanovich,[26] J. Ying,[23] S. Yokkaichi,[61,62] J. H. Yoo,[35] Z. You,[59] G. R. Young,[57] I. Younus,[39,54] H. Yu,[55] I. E. Yushmanov,[36] W. A. Zajc,[14] C. Zhang,[57] S. Zharko,[64] S. Zhou,[11] L. Zolin,[32] and L. Zou[8]
(PHENIX Collaboration)

[1]*Abilene Christian University, Abilene, Texas 79699, USA*
[2]*Department of Physics, Augustana University, Sioux Falls, South Dakota 57197, USA*
[3]*Department of Physics, Banaras Hindu University, Varanasi 221005, India*
[4]*Bhabha Atomic Research Centre, Bombay 400 085, India*
[5]*Baruch College, City University of New York, New York, New York 10010, USA*
[6]*Collider-Accelerator Department, Brookhaven National Laboratory, Upton, New York 11973-5000, USA*
[7]*Physics Department, Brookhaven National Laboratory, Upton, New York 11973-5000, USA*
[8]*University of California-Riverside, Riverside, California 92521, USA*
[9]*Charles University, Ovocný trh 5, Praha 1, 116 36, Prague, Czech Republic*
[10]*Chonbuk National University, Jeonju, 561-756, Korea*
[11]*Science and Technology on Nuclear Data Laboratory, China Institute of Atomic Energy, Beijing 102413, People's Republic of China*
[12]*Center for Nuclear Study, Graduate School of Science, University of Tokyo, 7-3-1 Hongo, Bunkyo, Tokyo 113-0033, Japan*
[13]*University of Colorado, Boulder, Colorado 80309, USA*
[14]*Columbia University, New York, New York 10027 and Nevis Laboratories, Irvington, New York 10533, USA*
[15]*Czech Technical University, Zikova 4, 166 36 Prague 6, Czech Republic*
[16]*Dapnia, CEA Saclay, F-91191, Gif-sur-Yvette, France*
[17]*Debrecen University, H-4010 Debrecen, Egyetem tér 1, Hungary*
[18]*ELTE, Eötvös Loránd University, H-1117 Budapest, Pázmány P. s. 1/A, Hungary*
[19]*Eszterházy Károly University, Károly Róbert Campus, H-3200 Gyöngyös, Mátrai út 36, Hungary*
[20]*Ewha Womans University, Seoul 120-750, Korea*
[21]*Florida Institute of Technology, Melbourne, Florida 32901, USA*
[22]*Florida State University, Tallahassee, Florida 32306, USA*
[23]*Georgia State University, Atlanta, Georgia 30303, USA*
[24]*Hiroshima University, Kagamiyama, Higashi-Hiroshima 739-8526, Japan*
[25]*Department of Physics and Astronomy, Howard University, Washington, DC 20059, USA*
[26]*IHEP Protvino, State Research Center of Russian Federation, Institute for High Energy Physics, Protvino 142281, Russia*
[27]*University of Illinois at Urbana-Champaign, Urbana, Illinois 61801, USA*
[28]*Institute for Nuclear Research of the Russian Academy of Sciences, prospekt 60-letiya Oktyabrya 7a, Moscow 117312, Russia*
[29]*Institute of Physics, Academy of Sciences of the Czech Republic, Na Slovance 2, 182 21 Prague 8, Czech Republic*
[30]*Iowa State University, Ames, Iowa 50011, USA*
[31]*Advanced Science Research Center, Japan Atomic Energy Agency, 2-4 Shirakata Shirane, Tokai-mura, Naka-gun, Ibaraki-ken 319-1195, Japan*
[32]*Joint Institute for Nuclear Research, 141980 Dubna, Moscow Region, Russia*
[33]*Helsinki Institute of Physics and University of Jyväskylä, P.O.Box 35, FI-40014 Jyväskylä, Finland*
[34]*KEK, High Energy Accelerator Research Organization, Tsukuba, Ibaraki 305-0801, Japan*
[35]*Korea University, Seoul 02841, Korea*
[36]*National Research Center "Kurchatov Institute," Moscow, 123098, Russia*
[37]*Kyoto University, Kyoto 606-8502, Japan*
[38]*Laboratoire Leprince-Ringuet, Ecole Polytechnique, CNRS-IN2P3, Route de Saclay, F-91128, Palaiseau, France*
[39]*Physics Department, Lahore University of Management Sciences, Lahore 54792, Pakistan*
[40]*Lawrence Livermore National Laboratory, Livermore, California 94550, USA*
[41]*Los Alamos National Laboratory, Los Alamos, New Mexico 87545, USA*
[42]*LPC, Université Blaise Pascal, CNRS-IN2P3, Clermont-Fd, 63177 Aubiere Cedex, France*
[43]*Department of Physics, Lund University, Box 118, SE-221 00 Lund, Sweden*
[44]*IPNL, CNRS/IN2P3, Univ Lyon, Université Lyon 1, F-69622, Villeurbanne, France*
[45]*University of Maryland, College Park, Maryland 20742, USA*
[46]*Department of Physics, University of Massachusetts, Amherst, Massachusetts 01003-9337, USA*
[47]*Department of Physics, University of Michigan, Ann Arbor, Michigan 48109-1040, USA*
[48]*Institut für Kernphysik, University of Münster, D-48149 Münster, Germany*
[49]*Muhlenberg College, Allentown, Pennsylvania 18104-5586, USA*
[50]*Myongji University, Yongin, Kyonggido 449-728, Korea*
[51]*Nagasaki Institute of Applied Science, Nagasaki-shi, Nagasaki 851-0193, Japan*
[52]*Nara Women's University, Kita-uoya Nishi-machi Nara 630-8506, Japan*
[53]*National Research Nuclear University, MEPhI, Moscow Engineering Physics Institute, Moscow 115409, Russia*

[54]*University of New Mexico, Albuquerque, New Mexico 87131, USA*
[55]*New Mexico State University, Las Cruces, New Mexico 88003, USA*
[56]*Department of Physics and Astronomy, Ohio University, Athens, Ohio 45701, USA*
[57]*Oak Ridge National Laboratory, Oak Ridge, Tennessee 37831, USA*
[58]*IPN-Orsay, Univ. Paris-Sud, CNRS/IN2P3, Université Paris-Saclay, BP1, F-91406, Orsay, France*
[59]*Peking University, Beijing 100871, People's Republic of China*
[60]*PNPI, Petersburg Nuclear Physics Institute, Gatchina, Leningrad Region, 188300, Russia*
[61]*RIKEN Nishina Center for Accelerator-Based Science, Wako, Saitama 351-0198, Japan*
[62]*RIKEN BNL Research Center, Brookhaven National Laboratory, Upton, New York 11973-5000, USA*
[63]*Physics Department, Rikkyo University, 3-34-1 Nishi-Ikebukuro, Toshima, Tokyo 171-8501, Japan*
[64]*Saint Petersburg State Polytechnic University, St. Petersburg 195251, Russia*
[65]*Universidade de São Paulo, Instituto de Física, Caixa Postal 66318, São Paulo CEP05315-970, Brazil*
[66]*Department of Physics and Astronomy, Seoul National University, Seoul 151-742, Korea*
[67]*Chemistry Department, Stony Brook University, SUNY, Stony Brook, New York 11794-3400, USA*
[68]*Department of Physics and Astronomy, Stony Brook University, SUNY, Stony Brook, New York 11794-3800, USA*
[69]*Sungkyunkwan University, Suwon 440-746, Korea*
[70]*University of Tennessee, Knoxville, Tennessee 37996, USA*
[71]*Department of Physics, Tokyo Institute of Technology, Oh-okayama, Meguro, Tokyo 152-8551, Japan*
[72]*Tomonaga Center for the History of the Universe, University of Tsukuba, Tsukuba, Ibaraki 305, Japan*
[73]*Vanderbilt University, Nashville, Tennessee 37235, USA*
[74]*Waseda University, Advanced Research Institute for Science and Engineering, 17 Kikui-cho, Shinjuku-ku, Tokyo 162-0044, Japan*
[75]*Weizmann Institute, Rehovot 76100, Israel*
[76]*Institute for Particle and Nuclear Physics, Wigner Research Centre for Physics, Hungarian Academy of Sciences (Wigner RCP, RMKI) H-1525 Budapest 114, POBox 49, Budapest, Hungary*
[77]*Yonsei University, IPAP, Seoul 120-749, Korea*

(Received 6 March 2018; revised manuscript received 14 December 2018; published 7 May 2019)

We present measurements of azimuthal correlations of charged hadron pairs in $\sqrt{s_{NN}} = 200$ GeV Au + Au collisions for the trigger and associated particle transverse-momentum ranges of $1 < p_T^t < 10$ GeV/c and $0.5 < p_T^a < 10$ GeV/c. After subtraction of an underlying event using a model that includes higher-order azimuthal anisotropy v_2, v_3, and v_4, the away-side yield of the highest trigger-p_T ($p_T^t > 4$ GeV/c) correlations is suppressed compared with that of correlations measured in $p + p$ collisions. At the lowest associated particle p_T ($0.5 < p_T^a < 1$ GeV/c), the away-side shape and yield are modified relative to those in $p + p$ collisions. These observations are consistent with the scenario of radiative-jet energy loss. For the low-p_T trigger correlations ($2 < p_T^t < 4$ GeV/c), a finite away-side yield exists and we explore the dependence of the shape of the away-side within the context of an underlying-event model. Correlations are also studied differentially versus event-plane angle Ψ_2 and Ψ_3. The angular correlations show an asymmetry when selecting the sign of the difference between the trigger-particle azimuthal angle and the Ψ_2 event plane. This asymmetry and the measured suppression of the pair yield out-of-plane is consistent with a path-length-dependent energy loss. No Ψ_3 dependence can be resolved within experimental uncertainties.

DOI: 10.1103/PhysRevC.99.054903

I. INTRODUCTION

Energy loss of hard-scattered partons (jet quenching [1]) resulting from the interaction of a colored parton in the quark gluon plasma (QGP) formed in relativistic heavy-ion collisions at the Relativistic Heavy Ion Collider (RHIC) [2–5] has been observed in several different ways. Suppression of single-particle and single-jet invariant yields in central $A + A$ collisions [6–12] provides a baseline measurement of jet quenching. Measurements of correlations between two particles and/or jets give more detailed information of the jet quenching process inside the medium [13,14]. The first jet suppression effect observed in azimuthal correlations was an attenuation of the away-side yields in high-transverse momenta (p_T) correlations in the most-central Au + Au collisions at $\sqrt{s_{NN}} = 200$ GeV [15]. The centrality dependence of high-$p_T \pi^0$-hadron correlations [16] shows a monotonic attenuation of the away-side yields with increasing propagation length of partons through the medium. In addition to away-side yield suppression, direct photon-hadron correlations [17–19], two-particle correlations [20–22], and

*Deceased.
†akiba@rcf.rhic.bnl.gov

jet-hadron correlations [23–26] show that low-momentum particles correlated with high-p_T jets are enhanced in yield, especially at large angles with respect to the jet axis. This may be attributable to the radiation from the parent parton or other lost energy absorbed by the surrounding medium. Thus, two-particle angular correlations have provided much of the experimental information we have about jet energy loss [16,27–31].

It is important to understand the interactions of partons with the QGP at all scales from the hard-scattering scale to the thermal scale. Below $E_{\rm jet} \approx 10$ GeV, full jet reconstruction is much more difficult due the underlying event subtraction. Two-particle correlations are important because they can probe lower jet (or parton) energies. However, observations of the energy-loss effects mentioned above, especially for lower jet and particle momenta in two-particle correlations, have been obscured due to the much larger contribution from the underlying event at these momenta.

The underlying event modulations are attributed to hydrodynamic collective flow patterns where the importance of higher-order flow harmonics was established more recently [32–37]. These patterns are thought to result from the hydrodynamic response of the QGP to fluctuating initial geometrical shapes of the overlap region of the colliding nuclei. Many hydrodynamic models have been developed which capture these effects [38,39] but, to date, important details of these models are still under development, and their full implementation requires involved calculations. This motivates the use of a simpler data-driven model, which will be explored in this work.

The shape of the collective flow in the transverse plane is parametrized [40–42] by a Fourier expansion with

$$v_n\{\Psi_m\} = \langle \cos n(\phi - \Psi_m) \rangle, \tag{1}$$

where v_n is the nth-order anisotropic flow coefficient, ϕ is the azimuthal angle of emitted particles, and Ψ_m is the event plane angle defined by the mth-harmonic number. For the first decade of RHIC operations, only the even harmonics and frequently only the $n = 2$ term, were considered. The shapes of two-particle correlations after subtraction of the ($n = 2$)-only background motivated the introduction of the other harmonics, most importantly $n = 3$ [32,34–36,43]. Under the two-source (flow + jet) model assumption [44], this underlying event is directly subtracted to obtain the jet contributions. In our previous measurements and most RHIC $A + A$ results, the subtracted flow modulations of the underlying event were limited to contributions of v_2 and the fourth-order harmonic component with respect to the second-order event plane $v_4\{\Psi_2\}$ [15,16,20,23,28,44–48]. Only the recent STAR measurement [49] took into account contributions from v_3 and the fourth-order harmonic component uncorrelated to the second-order event-plane in addition to $v_4\{\Psi_2\}$.

At low-to-intermediate p_T in two-particle correlations, intricate features appear such as the near-side long-range rapidity correlations called the "ridge" [45,50] and the away-side "double-humped" structures [28,44,46–49,51,52]. Across the large rapidity ranges available at the Large Hadron Collider, the rapidity-independence and hence the likely geometrical origin of most of these structures have been established. Experiments have shown that the ridge and the double-hump structures in the two-particle azimuthal correlations for $|\Delta\eta| > 1$ for ALICE and $|\Delta\eta| > 2$ for ATLAS and CMS measured in $p + p$, $p +$ Pb, and Pb + Pb collisions at $\sqrt{s_{NN}} =$ 2.76 and 5 TeV [34,36,53] are the same in shape and size at much larger rapidity differences. Both the ridge and double-hump are successfully explained by the higher-order harmonics. However, the mechanism for how the jet correlations combine with the flow correlations, especially at small $\Delta\eta$, to yield the total two-particle correlation has not been clarified. In particular, the correlations left after subtracting a flow-based model at small $\Delta\eta$ have not been analyzed in detail.

In this work, we assume a two-source model where the total pair yield is a sum of a jet-like component and an underlying-event component. The underlying-event components are modeled by using the flow harmonics v_n ($n =$ 2, 3, 4), event-plane resolutions, and the most important event plane correlations between Ψ_2 and Ψ_4. We assume that the v_n measured through the event-plane method are the same as those in the correlation functions. Event-by-event v_n fluctuations [54], v_n-v_m correlations between different orders [55], normalized symmetric cumulants (v_n^2-v_m^2 correlations) [56], and rapidity-dependent event-plane decorrelations [57] are not included in this background model. To take into account the v_n-v_m and v_n^2-v_m^2 correlations in this background model, measurements of their original two-dimensional probability distributions are necessitated for fine p_T selections. To evaluate a possible effect from the v_n-v_m and v_n^2-v_m^2 correlations, we performed a toy Monte Carlo simulation with the same framework reported in this article, assuming a two-dimensional Gaussian with a correlation term between v_n-v_m. The changes expected are less than the systematic uncertainty for v_n. Measurements of the rapidity-odd component of the directed flow $v_1^{\rm odd}$ using the event-plane method [58–61] generally yield $v_1^{\rm odd} \sim 0$ at $\eta = 0$ integrated over all p_T. Finite values of p_T differential measurements of $v_1^{\rm odd}(p_T)$ [60] include momentum conservation and jet (mini-jet) effects which are considered signal in this two-particle correlation analysis. The rapidity-event component of the directed flow $v_1^{\rm even}$ is considered to result from collective expansion of the medium. Measurements of $v_1^{\rm even}$ with respect to the spectator event plane with the scalar product method [62] show its magnitude to be about 40 times smaller than that with respect to the participant event plane obtained with the Fourier fits to the two-particle correlations [34,53]. These observations indicate that $v_1^{\rm even}$ has different sensitivity to the spectator and participant event planes and warrant further validation of the momentum conservation model in the Fourier fits to the two-particle correlations. There is currently no concrete $v_1^{\rm even}$ to subtract as background. With this reason we do not include contributions from $v_1\{\Psi_1\}$ and event-plane correlations involving Ψ_1 in the background model. For the inclusive trigger correlations, we estimated a potential impact of v_5 modulation using an empirical relation $v_5 \sim 0.5 v_4$ found in ATLAS v_n measurements [34].

After subtracting the underlying event with the model, we study the structures observed at high p_T where the flow backgrounds are negligible. Because the jet signal-to-flow background is significantly reduced in the low-to-intermediate-p_T region, studying the correlations there provides a more

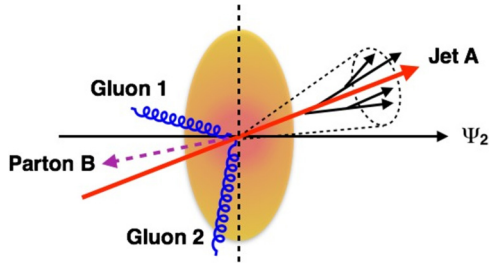

FIG. 1. Two possible gluons (Gluon 1 and Gluon 2) radiated opposite to particles detected from Jet A with different medium path lengths. The difference in energy loss could lead to asymmetric correlated particle yields in the hemisphere to the left of Jet A compared with the right of Jet A.

stringent test of such a background model. Any features left in the residuals can be used to reveal jet energy-loss effects at low and intermediate p_T. However, because of our simple model, only substantially significant correlations can be attributable to the medium effect on jets (i.e., broadening or suppression) or the medium response (i.e., yields at large angles from the jet).

An important goal of jet quenching studies has been to determine the density and path-length dependence of energy loss [16]. Perturbative models of radiative jet quenching and strongly coupled jet quenching models predict a different path-length dependence for the quenching [63]. Varying the path length by selecting azimuthal orientations relative to the second-order event plane has been explored for single-particle or single-jet observables at high p_T [11,64]. Potentially more differential information can be obtained from two-particle observables coupled with the event plane. Figure 1 illustrates the trigger (Jet A) being emitted to one side of the in-plane direction and the away-side jet (Parton B) radiating two gluons (Gluon 1) and (Gluon 2). Therefore, we also study two-particle correlations measured differentially with respect to the Ψ_2 and Ψ_3 event planes as depicted in Fig. 2. Such differential correlations probe the path-length and geometrical dependence of energy loss with more event-by-event sensitivity and also extend similar studies of high-p_T correlations [16] down to lower p_T. We use a new method of distinguishing "left-right"asymmetry in the Ψ_n correlations, which provides more information on the background-dominated low- and intermediate-p_T regions by probing possible asymmetric parton energy loss because of medium geometry.

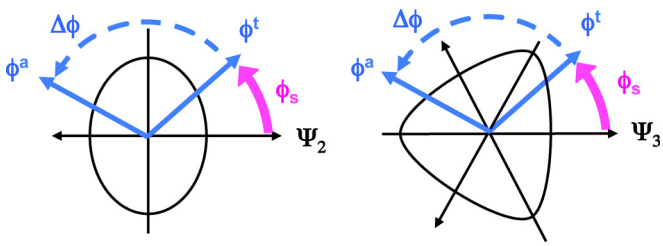

FIG. 2. Schematic picture of a trigger particle selection with respect to event planes and pairing a trigger particle with an associated particle.

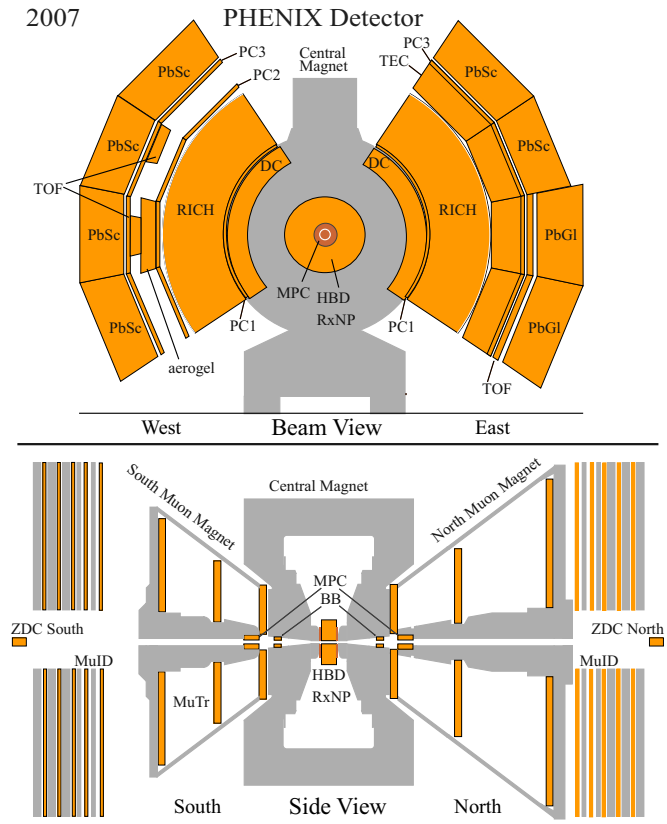

FIG. 3. The PHENIX detector configuration in the 2007 experimental run period. The top panel shows the central arm detectors viewed from the beam direction. The bottom panel shows the global detectors and muon arm viewed from the side perpendicular to the beam direction.

In this article, Sec. II describes the detector setup of the PHENIX experiment. Sections III A, III B, and III C describe the analysis methodology of particle selections, higher-order flow harmonics, and two-particle correlations, respectively. Section IV presents analysis results and discusses their interpretations. This section first starts with the highest p_T trigger selections, $p_T \gtrsim 4$ GeV/c, and makes connections to known energy-loss effects. Next, lower trigger correlations down to 1 GeV/c are presented. Finally the event-plane dependence of the intermediate-p_T selections are investigated. Section V summarizes this article.

II. PHENIX DETECTOR

The PHENIX detector [65] was designed to measure charged hadrons, leptons, and photons to study the nature of the QGP formed in ultrarelativistic heavy-ion collisions. Figure 3 shows the beam view and side view of the PHENIX detector including all subsystems for this data-taking period.

The global detectors, which include the beam-beam counters (BBCs), the zero-degree calorimeters (ZDCs), and the reaction-plane detector (RXN), were used to determine event-characterizing parameters such as the collision vertex, collision centrality, and event-plane orientation. They are located on both the south and north side of the PHENIX detectors.

The BBC is located at ± 144 cm$(3 < |\eta| < 3.9)$ from the beam interaction point and surrounds the beam pipe with full $\Delta\phi = 2\pi$ azimuthal acceptance. Each BBC module comprises 64 quartz Čerenkov radiators equipped with a photomultiplier tube (PMT) and measures the total charge (which is proportional to the number of particles) deposited in its acceptance. The BBC determines the beam collision time, beam collision position along the beam axis direction, and collision centrality. The ZDCs [66], located 18 m away from the nominal interaction point, detect the energy deposited by spectator neutrons of the two colliding nuclei. The PHENIX minimum-bias trigger is provided by the combination of hit information in the ZDC and BBC, which requires at least one hit in both the ZDC modules and two hits in the BBC modules.

The orientation of higher-order event planes is determined by the BBC and the RXN [67], which have different η acceptance. The RXNs are located at ± 38 cm from the beam interaction point and have two rings in each module; RXN-inner and RXN-outer are installed to cover $1.5 < |\eta| < 2.8$ and $1 < |\eta| < 1.5$, respectively. Each ring has 12 scintillators in its azimuthal angle acceptance $\Delta\phi = 2\pi$.

Charged hadron tracks are reconstructed in the PHENIX central arm spectrometer (CNT), which is comprised of two separate arms, east and west. Each arm covers $|\eta| < 0.35$ and $\Delta\phi = \pi/2$.

The PHENIX tracking system is composed of the drift chamber (DC) in addition to two layers of pad chambers (PC1 and PC3) in the east arm and three layers of pad chambers (PC1, PC2, and PC3) in the west arm. Momentum is determined by measuring the track curvature through the magnetic field by means of a Hough transform with hit information from the DC and PC1 with a momentum resolution of $\delta p/p = 1.3\% \oplus 1.2\% p$ [68]. Additional track position information is provided by the outer layers of the pad chambers and the electromagnetic calorimeter (EMCal), which are Lead Glass (PbGl) and Lead Scintillator (PbSc).

The ring imaging Čerenkov counter (RICH) and the EMCal identify and exclude electron tracks from the analysis. The RICH produces a light yield for electrons with $p_T > 30$ MeV and for pions with $p_T > 5$ GeV, meaning that a signal in the RICH can be used to separate electrons and pions below 5 GeV. Above 5 GeV where this is no longer possible, the energy deposited in the EMCal can be used for this separation. Electrons will deposit much more of their total energy than pions will, so that the ratio of deposited energy to track momentum is significantly higher for electrons than for pions.

III. ANALYSIS METHODOLOGY

The results presented are based on an analysis of 4.38 billion minimum-bias events for Au + Au collisions at $\sqrt{s_{NN}} = 200$ GeV recorded by the PHENIX detector at RHIC in 2007.

A. Particle selection

Charged hadrons are selected from candidate tracks by using cuts similar to previous correlation analyses [20]. One important cut to reject fake tracks, especially decays in the central magnetic field before the drift chamber, is an association cut to outer CNT detectors. The track trajectories are projected onto outer CNT detectors. The nearest hits in the PC3 and the EMCal from the projections are identified as hits for the track. The distributions of the distance in the azimuthal (ϕ) and beam ($z_{\rm beam}$) directions between the hits in the PC3 and the EMCal and the extrapolated line are fit with a double Gaussian. One Gaussian arises from the background and the other from the signal. Hadron tracks are required to be within $\pm 2\sigma$ of the signal Gaussian mean in both the ϕ and $z_{\rm beam}$ directions in both the PC3 and the EMCal. To veto conversion electrons, tracks with $p_T < 5$ GeV/c having one or more Čerenkov photons in the RICH are excluded from this analysis. For $p_T > 5$ GeV/c, we require $E_{\rm EMCal} > 0.3 + 0.2c \times p_T$ GeV [47,69], where $E_{\rm EMCal}$ is the cluster energy associated with the track.

B. Higher-order flow harmonics v_n

1. Event plane and resolution

Each event plane Ψ_n is determined event by event for different harmonic numbers n by using the RXN and BBC detectors. The RXN detectors are used to measure the nominal values of v_n while the BBC detectors provide systematic checks to the extracted v_n values. The observed event-plane $\Psi_n^{\rm obs}$ is reconstructed as

$$\Psi_n^{\rm obs} = \frac{1}{n}\tan^{-1}\left(\frac{Q_{n,y}}{Q_{n,x}}\right). \tag{2}$$

Here $Q_{n,x}$ and $Q_{n,y}$ are the flow vector components

$$Q_{n,x} = \sum_i w_i \cos(n\phi_i) \Big/ \sum_i w_i, \tag{3}$$

$$Q_{n,y} = \sum_i w_i \sin(n\phi_i) \Big/ \sum_i w_i, \tag{4}$$

where ϕ_i is the azimuthal angle of the ith segment in the event-plane detector and w_i is the weight proportional to multiplicity in the ith segment. We apply the recentering and the flattening corrections [42,70] separately for each subevent event plane.

The $k \times n$th-order resolution of the nth-order event plane is defined as $\mathrm{Res}\{kn, \Psi_n\} = \langle \cos kn(\Psi_n^{\rm obs} - \Psi_n)\rangle$ and can be expressed as [42]

$$\mathrm{Res}\{kn, \Psi_n\} = \frac{\sqrt{\pi}}{2\sqrt{2}}\chi_n e^{-\frac{\chi_n^2}{4}}\left[I_{\frac{k-1}{2}}\left(\frac{\chi_n^2}{4}\right) + I_{\frac{k+1}{2}}\left(\frac{\chi_n^2}{4}\right)\right], \tag{5}$$

where $\chi_n = v_n\sqrt{2M}$, M is the multiplicity used to determine the event plane Ψ_n, and I_k is the modified Bessel function of the first kind.

Because the north (N) and south (S) modules of a given event-plane detector have the same pseudorapidity coverage and see the same multiplicity and energy for symmetric nucleus-nucleus collisions, the north and south modules should have identical resolution in case of no detector biases. We obtain the event-plane resolution of an event-plane detector by using the two subevent method [42]:

$$\begin{aligned}\mathrm{Res}\{kn, \Psi_n\} &= \left\langle \cos kn\left(\Psi_n^{\rm obs} - \Psi_n\right)\right\rangle \\ &= \sqrt{\left\langle \cos kn\left(\Psi_n^{N,\rm obs} - \Psi_n^{S,\rm obs}\right)\right\rangle}.\end{aligned} \tag{6}$$

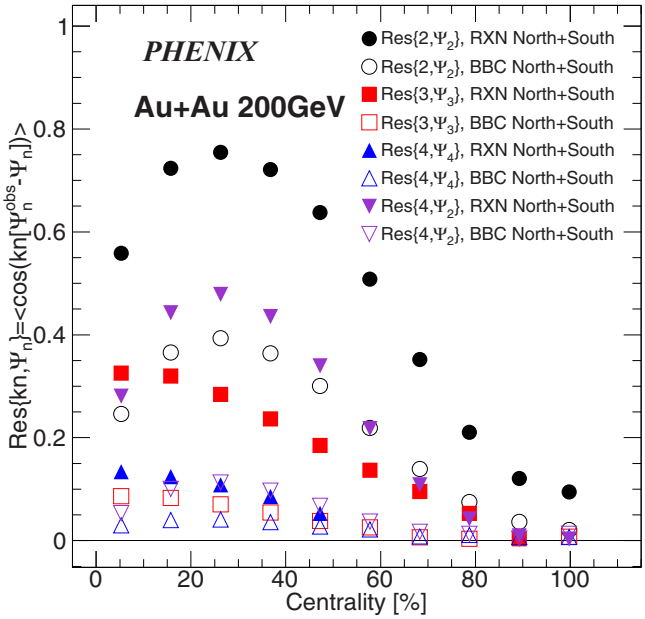

FIG. 4. Event-plane resolutions Res{2, Ψ_2}, Res{3, Ψ_3}, Res{4, Ψ_4}, and Res{4, Ψ_2} obtained by the combination of the north and south modules of RXN and BBC.

The north + south combined event-plane resolution is determined from Eq. (5) with $\chi_n = \sqrt{2}\chi_n^{N,S}$. The factor of $\sqrt{2}$ accounts for twice the multiplicity in north + south compared with north or south. Figure 4 shows the north + south combined event-plane resolution for both RXN and BBC.

2. v_n measurements

Higher-order flow harmonics v_n [32,40,42] are measured by the event-plane method [42]. Charged hadron tracks with azimuthal angle ϕ are measured with respect to the event-plane angle $\Psi_n^{\rm obs}$. The flow coefficients v_{kn} are measured as an event average and track average and corrected by the event-plane resolution:

$$v_{kn}\{\Psi_n\} = \left\langle \cos kn\left(\phi - \Psi_n^{\rm obs}\right)\right\rangle / {\rm Res}\{kn, \Psi_n\}. \tag{7}$$

Four different observables are studied: $v_2\{\Psi_2\}$, $v_3\{\Psi_3\}$, $v_4\{\Psi_4\}$, and $v_4\{\Psi_2\}$. The flow harmonics are measured by the nine possible combinations of RXN modules: south-inner, south-outer, south-inner + outer, north-inner, north-outer, north-inner + outer, south + north-inner, south + north-outer, and south + north-inner+outer. The v_n reported is an average over the nine different possible RXN combinations, $v_n = \sum_i^9 v_n^{(i)}/9$, where $v_n^{(i)}$ is the flow harmonic in one of the nine RXN module combinations.

3. Systematic uncertainties and v_n results

The systematic uncertainties in v_n measurements are from the following sources:

(1) differences among RXN modules;
(2) matching cut width for CNT hadron tracks;
(3) rapidity-separation dependence between event planes and CNT tracks.

The systematic uncertainties in the RXN detector $\sigma_{\rm RXN}$ are defined by the standard deviation of v_n

$$\sigma_{\rm RXN} = \sqrt{\sum_i^9 \left(v_n^{(i)} - v_n\right)^2/9}. \tag{8}$$

As an example, v_n in 20%–30% central collisions measured by different RXN event planes are shown in Figs. 5(a), 5(d), 5(g), and 5(j). The (blue) band indicates $\sigma_{\rm RXN}$.

To evaluate the systematic uncertainty due to track matching, the matching cut was varied by $\pm 0.5\sigma$ from the nominal 2σ window. We calculated the uncertainty $\sigma_{\rm mat}$ as the average deviation between the v_n with the nominal cut and the varied cut

$$\sigma_{\rm mat} = \left(\left|v_n^{2.5\sigma} - v_n^{2\sigma}\right| + \left|v_n^{1.5\sigma} - v_n^{2\sigma}\right|\right)/2. \tag{9}$$

The variation due to the track-matching cut is illustrated in Figs. 5(b), 5(e), 5(h), and 5(k) by showing v_n in 20%–30% central collisions measured with tracks having a matching cut of 1.5σ, 2σ, and 2.5σ. The differences between the nominal 2σ and both 1.5σ and 2.5σ are also shown and scatter around zero, indicating the size of $\sigma_{\rm mat}$.

The systematic uncertainties associated with the rapidity gap between particles and the event plane $\sigma_{\rm rap}$ are defined by the absolute difference between v_n determined by the RXN average and v_n determined by the BBC:

$$\sigma_{\rm rap} = \left|v_n^{\rm BBC} - v_n^{\rm RXN}\right|. \tag{10}$$

The v_n measured with the RXN, the BBC, and their difference are shown in Figs. 5(c), 5(f), 5(i), and 5(l). Except in the case of v_4, this systematic uncertainty is much less than the uncertainty due to the RXN module variation. The small variation in the rapidity gap indicates that the contamination from nonflow correlations does not dominate the uncertainty on the extraction of v_n.

The total systematic uncertainties σ_{v_n} are the quadrature sum of these individual systematic uncertainties,

$$\sigma_{v_n} = \sqrt{\sigma_{\rm RXN}^2 + \sigma_{\rm mat}^2 + \sigma_{\rm rap}^2}. \tag{11}$$

These total systematic uncertainties are conservatively assigned symmetrically. In nearly all p_T and centrality classes, the RXN systematic uncertainty dominates the total uncertainty.

The v_n results are shown in Fig. 6 and compared with previous PHENIX v_n measurements [35]. They are consistent within uncertainties where they overlap. For the two-particle correlations, we calculate v_n in four large p_T bins as indicated in Table I.

C. Two-particle correlations

1. Pair selections

Selected tracks are paired for correlations. Two tracks cannot be reconstructed arbitrarily close together. The

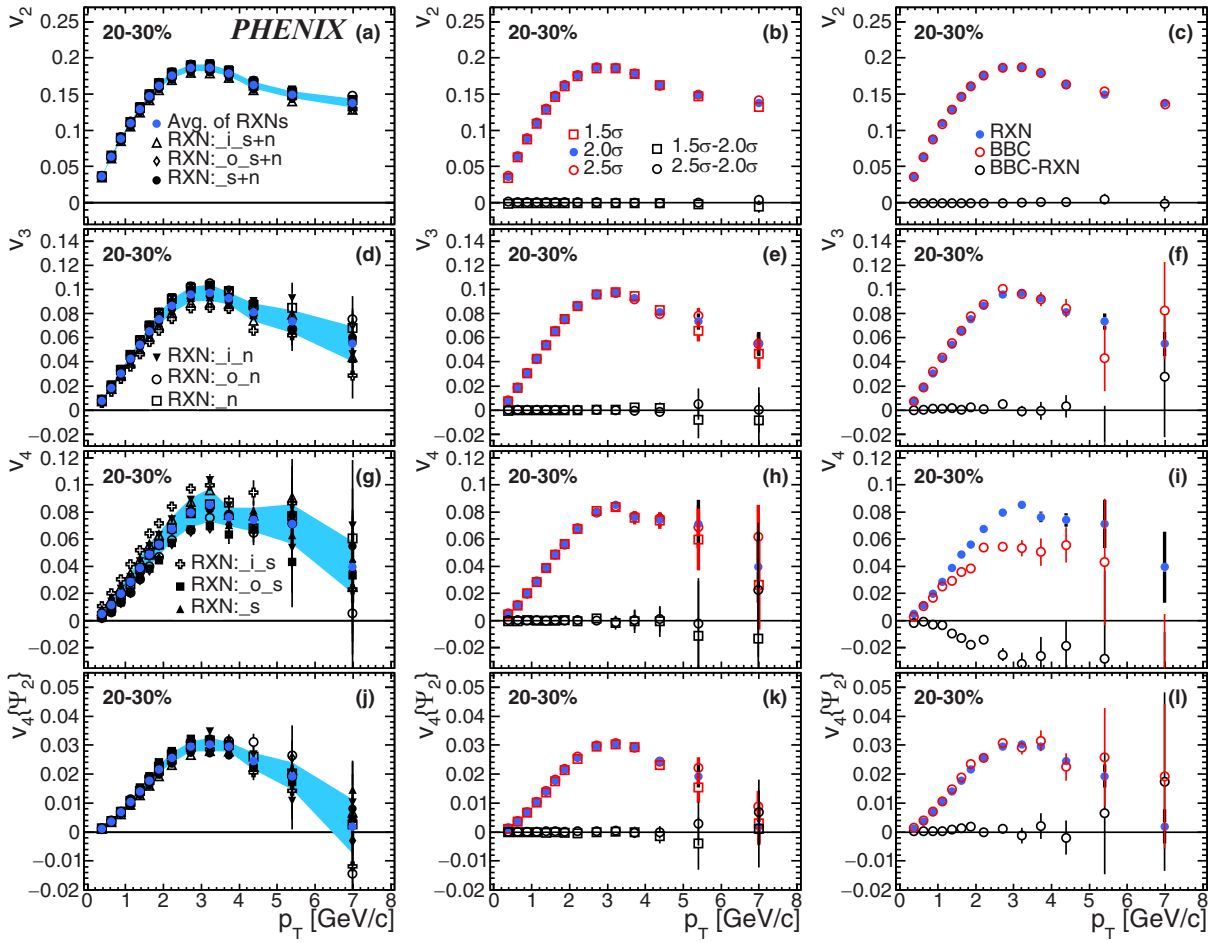

FIG. 5. Higher-order flow harmonics for charged hadrons at midrapidity in Au + Au collisions at $\sqrt{s_{NN}} = 200$ GeVand their systematics: (a)–(c) v_2, (d)–(f) v_3, (g)–(i) v_4, and (j)–(l) $v_4\{\Psi_2\}$ (j)–(l). (a), (d), (g), (j) The source of systematic uncertainties are different among RXN event planes; (b), (e), (h), (k) matching cut width for CNT hadron tracks; (c), (f), (i), (l) and difference between v_n measured with RXN and BBC event planes. Systematic uncertainties are shown as a shaded band in panels (a), (d), (g), (j) and as an open marker in panels (b), (e), (h), (k) and (c), (f), (i), (l).

tracking algorithm would split or merge the tracks. Therefore, there is an acceptance difference for pairs in real and mixed events. These effects are estimated from the distributions of the distances $\Delta\phi$ (rad) and $\Delta z_{\rm beam}$ (cm) between hits in the PC1 and the PC3, where $\Delta\phi$ (rad) is the relative azimuthal angle and $\Delta z_{\rm beam}$ (cm) is the relative length between two track hits in both real and mixed events. The ratios of the real-to-mixed event distributions are shown in Fig. 7. The ratio is normalized to arbitrary units. The dip and spike structures starting from $\Delta\phi = \Delta z_{\rm beam} = 0$ indicate inefficient and over-efficient regions, respectively. The dashed lines indicate the cuts used to remove these inefficient and over-efficient regions:

$$\sqrt{(\Delta\phi_{PC1}/0.04)^2 + (\Delta z_{{\rm beam},PC1}/90)^2} < 1,$$
$$\sqrt{(\Delta\phi_{PC1}/0.08)^2 + (\Delta z_{{\rm beam},PC1}/8.0)^2} < 1, \qquad (12)$$
$$\sqrt{(\Delta\phi_{PC3}/0.07)^2 + (\Delta z_{{\rm beam},PC3}/25)^2} < 1.$$

2. *Inclusive trigger correlations*

Two-particle correlations are calculated as

$$C(\Delta\phi) = \frac{N^{\rm real}(\Delta\phi)}{N^{\rm mixed}(\Delta\phi)} \frac{\int d\Delta\phi' N^{\rm mixed}(\Delta\phi')}{\int d\Delta\phi' N^{\rm real}(\Delta\phi')}, \qquad (13)$$

where $\Delta\phi = \phi^a - \phi^t$ is the relative azimuthal angle between trigger and associated hadrons and $N^{\rm real}(\Delta\phi)$ and $N^{\rm mixed}(\Delta\phi)$ are pair distributions in the real and mixed events, respectively. $N^{\rm real}(\Delta\phi)$ reflects the physical correlation among trigger and associated hadrons from jets and from the underlying event as well as the dihadron detector acceptance effects. $N^{\rm mix}(\Delta\phi)$ is obtained by pairing trigger and associated hadrons from randomly selected pairs of events that have similar collision vertices and centralities so that it reflects only the dihadron acceptance effects. The collision centrality is divided into 10% steps and the collision vertex in the range of ± 30 cm is divided into 10 bins for this event-mixing. Taking the ratio between the real and mixed distributions corrects for the nonuniform azimuthal acceptance for dihadrons so that $C(\Delta\phi)$ contains only physical effects.

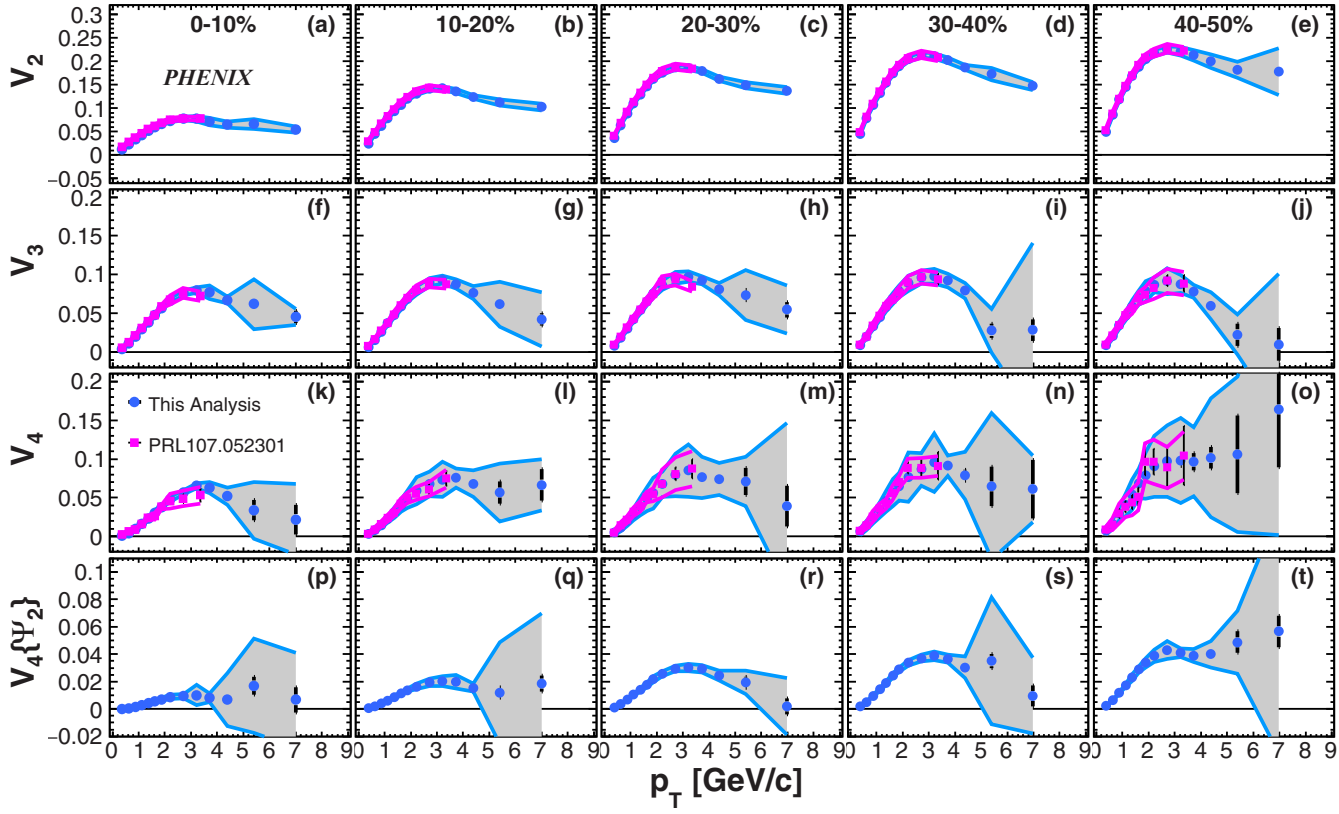

FIG. 6. Higher-order flow harmonics for charged hadrons at midrapidity in Au + Au collisions at $\sqrt{s_{NN}} = 200$ GeV. Coefficients are determined by using the event-plane method for (a)–(e) v_2, (f)–(j) v_3, (k)–(o) v_4, and (p)–(t) $v_4\{\Psi_2\}$. The columns represent centrality bins (a), (f), (k), (p) 0%–10%; (b), (g), (l), (q) 10%–20%; (c), (h), (m), (r) 20%–30%; (d), (i), (n), (s) 30%–40%; and (e), (j), (o), (t) 40%–50%. Coefficients obtained in this analysis are shown by blue points and those measured in Ref. [35] are shown by magenta points. Shaded bands and magenta lines indicate systematic uncertainties of those measurements.

TABLE I. Data table for v_2, v_3, v_4, and $v_4\{\Psi_2\}$ (%) in Au + Au collisions at $\sqrt{s_{NN}} = 200$ GeV. The first uncertainties are statistical while the second uncertainties are total systematic. In all instances the statistical error is not identically zero but it is much smaller than the systematic uncertainty.

Centrality	p_T GeV/c	v_2(%)	v_3(%)	v_4(%)	$v_4\{\Psi_2\}$(%)
0%–10%	0.5–1.0	$2.67 \pm 0.00 \pm 0.14$	$1.45 \pm 0.00 \pm 0.09$	$0.64 \pm 0.01 \pm 0.16$	$0.109 \pm 0.004 \pm 0.052$
	1.0–2.0	$4.92 \pm 0.00 \pm 0.21$	$3.67 \pm 0.00 \pm 0.18$	$2.19 \pm 0.01 \pm 022$	$0.396 \pm 0.005 \pm 0.058$
	2.0–4.0	$7.39 \pm 0.00 \pm 0.34$	$6.96 \pm 0.01 \pm 0.29$	$5.12 \pm 0.01 \pm 0.23$	$0.90 \pm 0.01 \pm 0.10$
	4.0–10	$6.46 \pm 0.00 \pm 0.67$	$6.61 \pm 0.01 \pm 0.41$	$5.0 \pm 0.0 \pm 1.1$	$0.7 \pm 0.0 \pm 1.4$
10%–20%	0.5–1.0	$5.09 \pm 0.00 \pm 0.19$	$1.94 \pm 0.00 \pm 0.16$	$1.04 \pm 0.01 \pm 0.30$	$0.270 \pm 0.003 \pm 0.033$
	1.0–2.0	$9.03 \pm 0.00 \pm 0.26$	$4.59 \pm 0.00 \pm 0.30$	$2.95 \pm 0.01 \pm 0.60$	$0.82 \pm 0.00 \pm 0.10$
	2.0–4.0	$13.4 \pm 0.0 \pm 0.04$	$8.28 \pm 0.01 \pm 0.51$	$6.2 \pm 0.0 \pm 1.7$	$1.74 \pm 0.00 \pm 0.24$
	4.0–10	$12.2 \pm 0.0 \pm 0.04$	$7.5 \pm 0.0 \pm 1.0$	$6.7 \pm 0.0 \pm 1.3$	$1.54 \pm 0.01 \pm 0.50$
20%–30%	0.5–1.0	$7.26 \pm 0.00 \pm 0.20$	$2.29 \pm 0.00 \pm 0.22$	$1.44 \pm 0.01 \pm 0.51$	$0.481 \pm 0.003 \pm 0.046$
	1.0–2.0	$12.5 \pm 0.0 \pm 0.3$	$5.17 \pm 0.01 \pm 0.40$	$3.6 \pm 0.0 \pm 1.0$	$1.33 \pm 0.00 \pm 0.11$
	2.0–4.0	$17.9 \pm 0.0 \pm 0.4$	$8.93 \pm 0.01 \pm 0.61$	$7.2 \pm 0.0 \pm 2.0$	$2.69 \pm 0.00 \pm 0.18$
	4.0–10	$16.1 \pm 0.0 \pm 0.5$	$7.98 \pm 0.01 \pm 0.76$	$7.3 \pm 0.0 \pm 2.4$	$2.34 \pm 0.01 \pm 0.28$
30%–40%	0.5–1.0	$8.83 \pm 0.00 \pm 0.22$	$2.49 \pm 0.01 \pm 0.31$	$1.79 \pm 0.02 \pm 0.64$	$0.682 \pm 0.004 \pm 0.050$
	1.0–2.0	$14.9 \pm 0.0 \pm 0.4$	$5.52 \pm 0.01 \pm 0.53$	$4.3 \pm 0.0 \pm 1.3$	$1.84 \pm 0.00 \pm 0.12$
	2.0–4.0	$20.7 \pm 0.0 \pm 0.5$	$9.13 \pm 0.01 \pm 0.88$	$8.1 \pm 0.0 \pm 3.0$	$3.49 \pm 0.01 \pm 0.21$
	4.0–10	$18.4 \pm 0.0 \pm 0.5$	$7.4 \pm 0.0 \pm 1.1$	$7.7 \pm 0.0 \pm 3.4$	$3.01 \pm 0.01 \pm 0.96$
40%–50%	0.5–1.0	$9.76 \pm 0.00 \pm 0.25$	$2.56 \pm 0.01 \pm 0.35$	$2.11 \pm 0.04 \pm 0.70$	$0.823 \pm 0.006 \pm 0.052$
	1.0–2.0	$16.3 \pm 0.0 \pm 0.4$	$5.62 \pm 0.01 \pm 0.68$	$5.2 \pm 0.0 \pm 1.8$	$2.19 \pm 0.01 \pm 0.14$
	2.0–4.0	$21.9 \pm 0.0 \pm 0.7$	$8.8 \pm 0.0 \pm 1.0$	$9.3 \pm 0.1 \pm 4.2$	$3.99 \pm 0.01 \pm 0.43$
	4.0–10	$19.8 \pm 0.0 \pm 1.6$	$5.6 \pm 0.0 \pm 1.9$	$10.4 \pm 0.1 \pm 8.0$	$4.1 \pm 0.0 \pm 1.2$

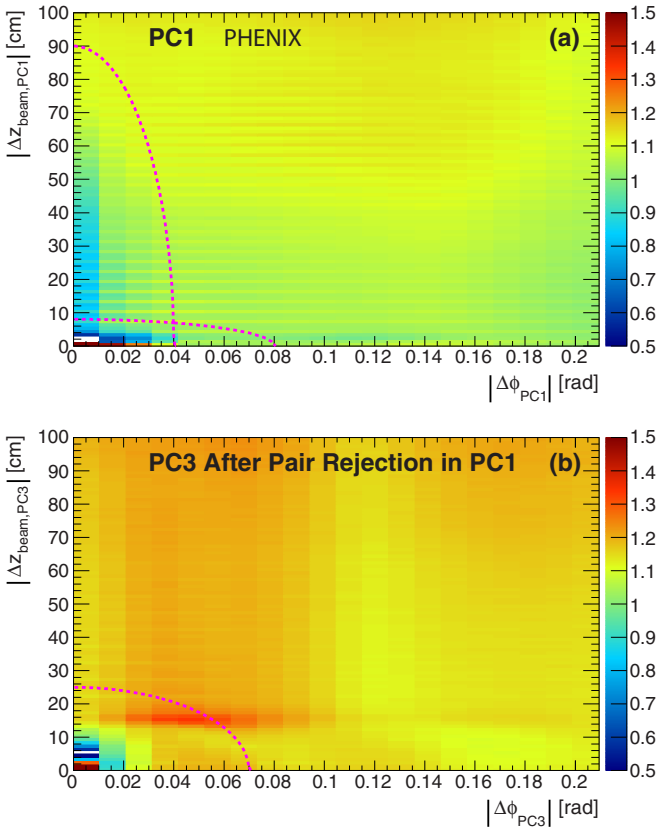

FIG. 7. The ratio of the real-event to mixed-event distributions of distances Δz_{beam}-$\Delta\phi$ between hits in a pair of tracks in (a) PC1 and (b) PC3 after the PC1 cut. The region encircled by dashed (magenta) curves are excluded from this analysis.

Within the two-source model [44], the correlation function $C(\Delta\phi)$ is composed of a jet-like term $J(\Delta\phi)$ and an underlying-event term that includes modulations from flow $F(\Delta\phi)$. We use the following model for the underlying event [42]:

$$F(\Delta\phi) = 1 + \sum_{n=2}^{4} 2v_n^t v_n^a \cos n\Delta\phi. \quad (14)$$

The jet-like correlation is then obtained by subtracting $F(\Delta\phi)$ from $C(\Delta\phi)$ as

$$J(\Delta\phi) = C(\Delta\phi) - b_{zyam}F(\Delta\phi). \quad (15)$$

The scaling factor b_{zyam} is determined with the zero yield at minimum (ZYAM) method [44,71,72]. In the ZYAM assumption, $F(\Delta\phi)$ is scaled such that $J(\Delta\phi)$ has a minimum of exactly zero. This therefore gives the lower boundary of possible jet-like correlations. The ZYAM scaling factor b_{zyam} is determined by fitting the correlation function $C(\Delta\phi)$ with Fourier series for $-\frac{\pi}{2} < \Delta\phi < \frac{3\pi}{2}$ and identifying the single point where this fit and $F(\Delta\phi)$ have the contact point and $J(\Delta\phi)$ is zero. The statistical uncertainty e_{zyam} of the $\Delta\phi$ bin containing the ZYAM point is used to scale $F(\Delta\phi)$ to estimate the systematic uncertainty due to ZYAM,

$$\sigma_{zyam}(\Delta\phi) = e_{zyam}F(\Delta\phi). \quad (16)$$

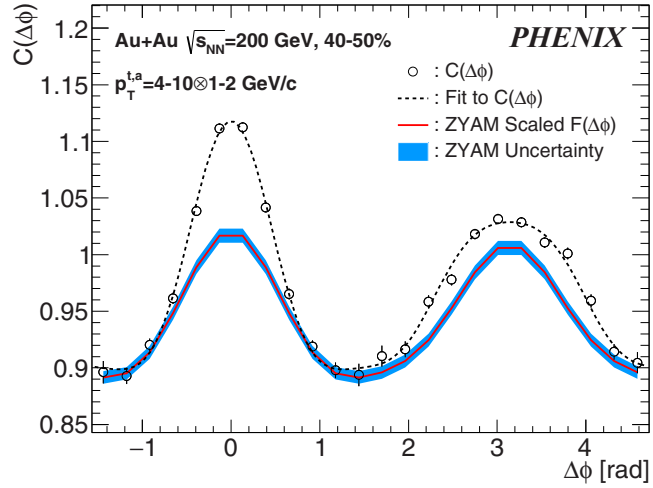

FIG. 8. Example of ZYAM extraction where the correlation function $C(\Delta\phi)$ (open circle) is fitted (dashed line). The normalization of the underlying event model (red solid line) is adjusted to match the minimum value of the fit. The (blue) band indicates the uncertainty on the ZYAM extraction determined by the statistical uncertainty of $C(\Delta\phi)$ near the minimum.

An example of the ZYAM determination is shown in Fig. 8.

The jet-like correlations $J(\Delta\phi)$ are scaled to the per-trigger yield $Y(\Delta\phi)$:

$$Y(\Delta\phi) = \frac{1}{N^t}\frac{dN^{ta}}{d\Delta\phi} = \frac{\int d\Delta\phi' N^{\text{real}}(\Delta\phi')}{2\pi\epsilon^a N^t} J(\Delta\phi'), \quad (17)$$

where N^t is the number of trigger hadrons, N^{ta} is the number of pairs, and ϵ^a is the single-hadron tracking efficiency in the associated hadron p_T range. The efficiency is estimated via detector simulations for acceptance and occupancy effects as discussed in Refs. [7,16,28,47]. The tracking efficiency of a trigger particle is canceled by the ratio $\int d\Delta\phi N^{\text{real}}/N^t$.

3. *Event-plane-dependent correlations*

Event-plane-dependent two-particle correlations $C(\Delta\phi, \phi_s)$ are defined as

$$C(\Delta\phi, \phi_s) = \frac{N^{\text{real}}(\Delta\phi, \phi_s)}{N^{\text{mixed}}(\Delta\phi, \phi_s)} \frac{\int\int d\Delta\phi' d\phi_s' N^{\text{mixed}}(\Delta\phi', \phi_s')}{\int\int d\Delta\phi' d\phi_s' N^{\text{real}}(\Delta\phi', \phi_s')}, \quad (18)$$

where $\phi_s = \phi^t - \Psi_n$ and $N^{\text{real}}(\Delta\phi, \phi_s)$ and $N^{\text{mix}}(\Delta\phi, \phi_s)$ are the event-plane-dependent pair $\Delta\phi$ distributions in real and mixed events, respectively. We use the event plane determined by the entire RXN acceptance, providing the best event-plane resolution among PHENIX subsystems, i.e., the best sensitivity for this event-plane-dependence study. Other event planes were not used because those planes have worse resolution.

Similar to inclusive correlations, event-plane-dependent jet-like correlations $J(\Delta\phi, \phi_s)$ are obtained by subtracting the event-plane-dependent flow background term $F(\Delta\phi, \phi_s)$ from $C(\Delta\phi, \phi_s)$ with a ZYAM scale factor as

$$J(\Delta\phi, \phi_s) = C(\Delta\phi, \phi_s) - b_{zyam}F(\Delta\phi, \phi_s). \quad (19)$$

We use the same b_{zyam} as determined from the inclusive correlations from the same trigger, associated, and centrality selection. An analytical formula for $F(\Delta\phi, \phi_s)$ including the $n = 2$ event-plane dependence exists [73]; however, it is not easily applied with finite correlations between the $n = 2$ and $n = 4$ event planes. For this reason, a Monte Carlo simulation is employed to estimate $F(\Delta\phi, \phi_s)$. This is described in Sec. III C 4 below.

The event-plane-dependent jet-like correlations are converted into event-plane-dependent per-trigger yield as

$$Y(\Delta\phi, \phi_s) = \frac{1}{N^t_{\phi_s}} \frac{dN^{ta}_{\phi_s}}{d\Delta\phi} = \frac{\int d\Delta\phi' N^{\text{real}}(\Delta\phi', \phi_s)}{2\pi\epsilon^a N^t_{\phi_s}} J(\Delta\phi', \phi_s), \tag{20}$$

where $N^t_{\phi_s}$ is the number of trigger hadrons and $N^{ta}_{\phi_s}$ is the number of pairs in the trigger event-plane bin.

4. Flow background model including event-plane dependence

With the assumption that the measured v_n from the event-plane method are purely from collective dynamics of the medium, flow-like azimuthal distributions of single hadrons can be generated by performing a Monte Carlo simulation, inputting the experimentally measured v_n, the resolution of the event planes, and the strength of correlation among different-order event planes. The single-hadron azimuthal distributions due to collective flow can be described by a superposition of v_n as

$$\frac{dN}{d\phi} = 1 + \sum_{n=2}^{4} 2v_n \cos n\left(\phi - \Psi_n^{\text{true}}\right), \tag{21}$$

where ϕ is the azimuthal angle of the emitted hadrons and Ψ_n^{true} is a true nth-order event plane defined over $[-\pi/n, \pi/n]$. Separate distributions using v_n for each p_T ranges of trigger and associated particles are used in the simulation. The trigger and associated distributions in real events share a common Ψ_n, while those in mixed events do not.

The experimental event-plane resolution is introduced through a dispersion term $\Delta\Psi_n$ where $\Psi_n^{\text{obs}} = \Psi_n^{\text{true}} + \Delta\Psi_n$. We calculate $\Delta\Psi_n$ as

$$\Delta\Psi_n = \frac{e^{-\frac{\chi_n^2}{2}}}{\pi}\left[1 + z_n\sqrt{\pi}[1 + \text{erf}(z_n)]e^{z_n^2}\right], \tag{22}$$

where $z_n = \chi_n/\sqrt{2}\cos(n\Delta\Psi_n)$ and $\text{erf}(z_n)$ is the error function [42,74]. This equation can be solved for $\Delta\Psi_n$ by using the experimentally determined χ_n from the measured event-plane resolutions using Eq. (5).

Because a weak correlation between Ψ_2^{true} and Ψ_3^{true} exists [35], the directions of Ψ_2^{true} and Ψ_3^{true} are generated independently. The direction of Ψ_4^{true} is generated by assuming a correlation with Ψ_2^{true}, $\Psi_4^{\text{true}} = \Psi_2^{\text{true}} + \Delta\Psi_{42}$. We estimate $\Delta\Psi_{42}$ by assuming that the correlation between the two event planes follows similar functional forms as the dispersion of event planes due to the resolution. That is, we assume

$$\Delta\Psi_{42} = \frac{e^{-\frac{\chi_{42}^2}{2}}}{\pi}\left[1 + z_{42}\sqrt{\pi}[1 + \text{erf}(z_{42})]e^{z_{42}^2}\right], \tag{23}$$

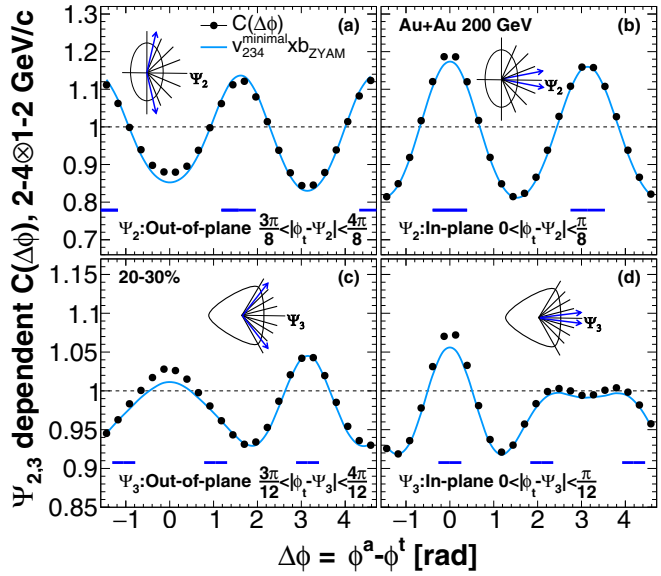

FIG. 9. Event-plane-dependent $C(\Delta\phi)$ (black circles) and event-plane-dependent model flow background (blue lines) of $(2 < p_T^t < 4) \otimes (1 < p_T^a < 2)$ GeV/c. Trigger particles are selected in (a) out-of-plane $3\pi/8 < |\phi^t - \Psi_2| < 4\pi/8$ of Ψ_2, (b) in-plane $0 < |\phi^t - \Psi_2| < \pi/8$ of Ψ_2, (c) out-of-plane $3\pi/12 < |\phi^t - \Psi_3| < 4\pi/12$ of Ψ_3, and (d) in-plane $0 < |\phi^t - \Psi_3| < \pi/12$ of Ψ_3. Schematic pictures in each panel also depict these ranges of the trigger-particle selections with respect to event plane Ψ_n.

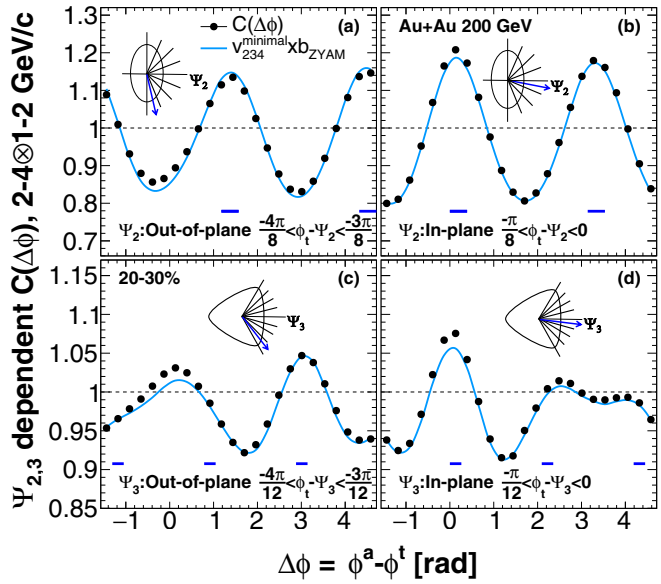

FIG. 10. Event-plane-dependent $C(\Delta\phi)$ (black circles) and event-plane-dependent model flow background (blue lines) of $(2 < p_T < 4) \otimes (1 < p_T^a < 2)$ GeV/c. Trigger particles are selected in (a) out-of-plane $-4\pi/8 < \phi^t - \Psi_2 < -3\pi/8$ of Ψ_2, (b) in-plane $-\pi/8 < \phi^t - \Psi_2 < 0$ of Ψ_2, (c) out-of-plane $-4\pi/12 < \phi^t - \Psi_3 < -3\pi/12$ of Ψ_3, and (d) in-plane $-\pi/12 < \phi^t - \Psi_3 < 0$ of Ψ_3. Schematic pictures in each panel also depict these ranges of the trigger-particle selections with respect to event plane Ψ_n.

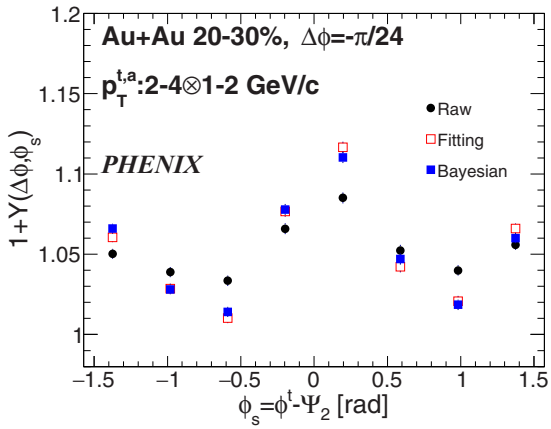

FIG. 11. The raw event-plane-dependent per-trigger yields offset by 1, $1 + Y(\Delta\phi = -\pi/24, \phi_s)$ (black circles). The resulting corrected per-trigger yields using iterative Bayesian unfolding (blue filled squares) and from Fourier fitting (red open squares).

where $z_{42} = \chi_{42}/\sqrt{2}\cos 4\Delta\Psi_{42}$. The parameter χ_{42} is assumed to be similar to Eq. (5):

$$\langle\cos(4\Delta\Psi_{42})\rangle = \frac{\sqrt{\pi}}{2\sqrt{2}}\chi_{42}e^{-\chi_{42}^2/4}\left[I_0\left(\frac{\chi_{42}^2}{4}\right) + I_1\left(\frac{\chi_{42}^2}{4}\right)\right], \tag{24}$$

where $\langle\cos(4\Delta\Psi_{42})\rangle = v_4\{\Psi_2\}/v_4$ [75]. The functional shape of Eq. (23) is verified by event-plane-correlation studies by using the BBCs and the RXNs following the method described in Ref. [76]. The correlation strength between $\Psi_2^{\rm true}$ and $\Psi_3^{\rm true}$, $\langle\cos 6(\Psi_2 - \Psi_3)\rangle$, is measured to be consistent with zero within large statistical uncertainties. Potential impacts of $\langle\cos 6(\Psi_2 - \Psi_3)\rangle$ to the event-plane-dependent correlations are estimated by using the value of $\langle\cos 6(\Psi_2 - \Psi_3)\rangle$ reported in Ref. [76] by the ATLAS experiment. The impact of $\langle\cos 6(\Psi_2 - \Psi_3)\rangle$ is within the systematic uncertainties described later.

We use the averaged χ_{42} value between $2 < p_T < 4$ GeV/c and $1 < p_T < 2$ GeV/c for event-plane-dependent correlations of $(2 < p_T^t < 4) \otimes (1 < p_T^a < 2)$, $(2 < p_T^t < 4) \otimes (2 < p_T^a < 4)$, and $(4 < p_T^t < 10) \otimes (2 < p_T^a < 4)$ GeV/c because $\langle\cos(4\Delta\Psi_{42})\rangle$ would contain autocorrelations from jets at high p_T.

The event-plane-dependent background shapes are determined by generated particles in this simulation by using Eq. (18). Figure 9 shows event-plane-dependent correlations and backgrounds with a selection of the absolute trigger azimuthal angle relative to the event planes $|\phi^t - \Psi_n|$. The backgrounds agree with the experimental correlations except at $\Delta\phi = 0, \pi$ where contributions from jets are expected. Figure 10 shows event-plane-dependent correlations and backgrounds with a selection of trigger azimuthal angle relative to event planes $\phi^t - \Psi_n < 0$. Agreement between the experimental correlations and the background except at

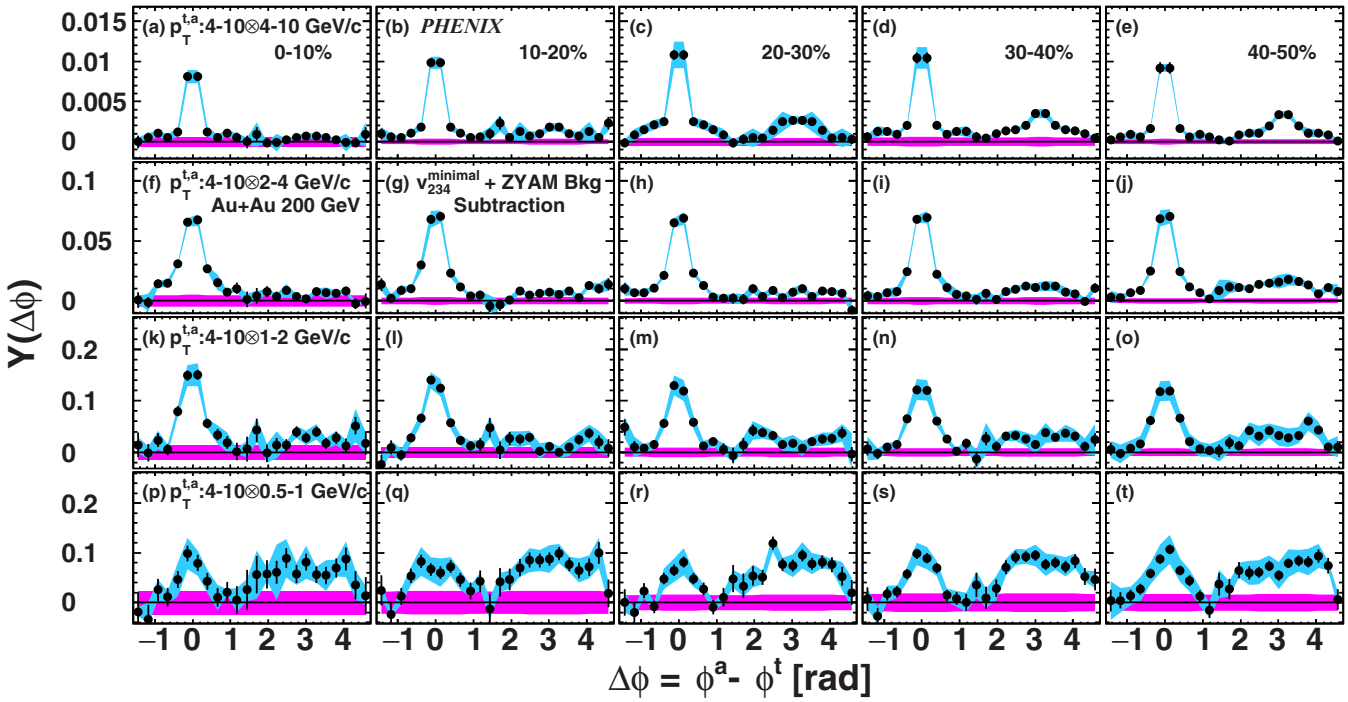

FIG. 12. Per-trigger yields $Y(\Delta\phi)$ of dihadron pairs measured in Au + Au collisions at $\sqrt{s_{NN}} = 200$ GeVafter subtracting the underlying event model with several p_T selections: (a)–(e) $(4 < p_T^t < 10) \otimes (4 < p_T^a < 10)$ GeV/c, (f)–(j) $(4 < p_T^t < 10) \otimes (2 < p_T^a < 4)$ GeV/c, (k)–(o) $(4 < p_T^t < 10) \otimes (1 < p_T^a < 2)$ GeV/c, and (p)–(t) $(4 < p_T^t < 10) \otimes (0.5 < p_T^a < 1)$ GeV/c. The columns represent centrality bins (a), (f), (k), (p) 0%–10%; (b), (g), (l), (q) 10%–20%; (c), (h), (m), (r) 20%–30%; (d), (i), (n), (s) 30%–40%; (e), (j), (o), (t) 40%–50%. Systematic uncertainties due to track matching and the v_n are shown by blue bands around the points. Uncertainties from ZYAM are shown by the purple bands around zero yield.

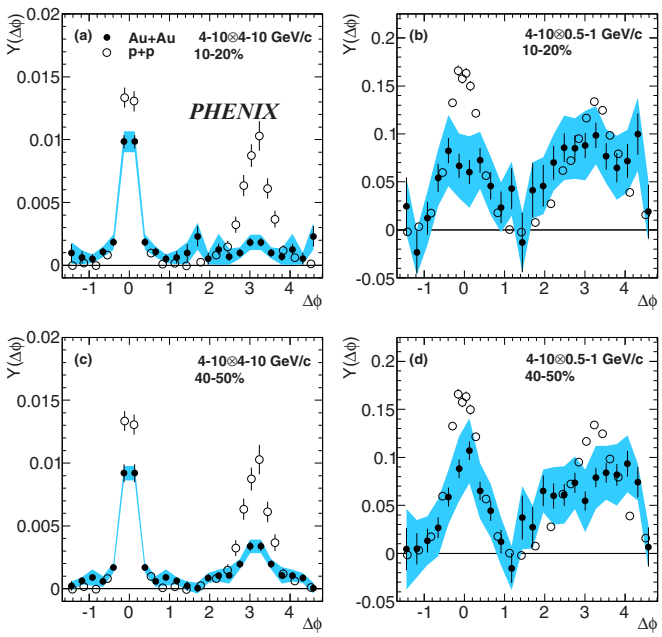

FIG. 13. Comparison per-trigger yields between Au + Au and $p + p$ collisions at $\sqrt{s_{NN}} = 200$ GeVfrom 4–10 GeV/c triggers correlated with associated particles (a), (c) 4–10 GeV/c and (b), (d) 0.5–1 GeV/c in (a), (b) 10%–20% and (c), (d) 40%–50% collisions after subtraction of the underlying-event model. In the highest associated p_T correlations an away-side suppression is observed. In the lowest associated p_T correlations an enhanced yield at angles far from $\Delta\phi = \pi$ is observed. The background normalization (ZYAM) uncertainty shown in the purple band around zero in Fig. 12 is included in the blue band around the points in this figure.

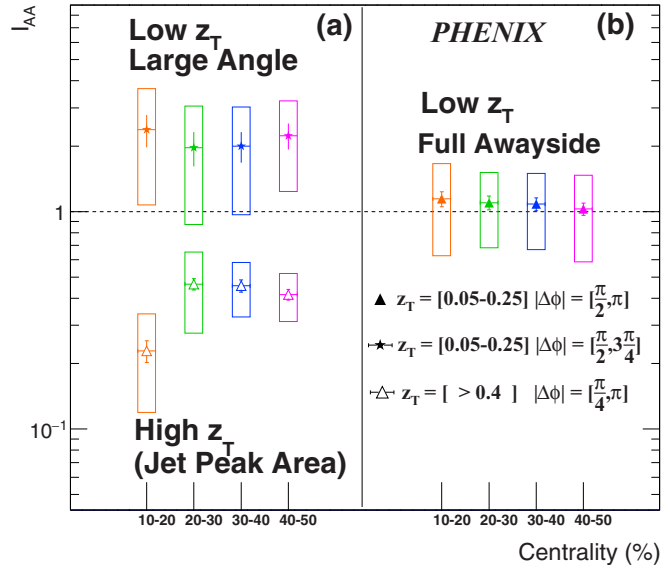

FIG. 14. I_{AA}: Ratio of away-side yields in Au + Au to $p + p$ from Fig. 13 in various $\Delta\phi$ integration regions for the high and low $z_T = p_T^a/p_T^t$. Away-side yields show the well-known suppression at high z_T, most pronounced for the small-angle region around the usual away-side peak center $|\Delta\phi - \pi| < \pi/4$. At low z_T, the large-angle integration region, $|\Delta\phi - \pi| > \pi/4$, shows an enhancement in I_{AA}, which is significantly higher than the high z_T suppressed values, and generally enhanced above unity. The full away-side integration region at low z_T is also higher than the suppressed level with at least 1σ significance for most centrality bins.

$\Delta\phi = 0, \pi$ is also observed here. Other event-plane-dependent correlations and backgrounds with a selection of trigger azimuthal angle relative to event planes $\phi^t - \Psi_n < 0$ for different collision centralities and $p_T^{t,a}$ selections are shown in the Appendix.

D. Unfolding of event-plane-dependent correlations

In this analysis, ϕ_s is divided into eight bins. The width of the ϕ_s bins is $\pi/8$ and $\pi/12$ when correlating with Ψ_2 and Ψ_3, respectively. The event-plane-dependent per-trigger yields $Y(\Delta\phi, \phi_s)$ are smeared across neighboring event-plane bins due to limited experimental resolution of the event planes. We unfold the smearing to obtain the true event-plane dependence of the correlations. Two different methods are used to check the unfolding procedure: (I) iterative Bayesian unfolding, $Y_{\rm unf}^{\rm itr}$, and (II) correcting the event-plane-dependence of the per-trigger yield based on a Fourier analysis, $Y_{\rm unf}^{\rm fit}$.

1. Iterative Bayesian unfolding

The iterative Bayesian unfolding method presented in Refs. [77,78] is applied to this analysis with the following formulation:

$$\hat{n}(\Delta\phi, \phi_{s,i}) = \sum_j M_{ij} n^{\rm obs}(\Delta\phi, \phi_{s,j}), \tag{25}$$

$$M_{ij} = \frac{P(\phi_{s,j}|\phi_{s,i}) n(\Delta\phi, \phi_{s,i})}{\varepsilon_i \sum_l P(\phi_{s,j}|\phi_{s,l}) n(\Delta\phi, \phi_{s,l})}, \tag{26}$$

where $\hat{n}(\Delta\phi, \phi_s)$ is the unfolded distribution, $n^{\rm obs}(\Delta\phi, \phi_s)$ is the experimentally observed distribution, $n(\Delta\phi, \phi_s)$ is the prior distribution, $P(\phi_{s,j}|\phi_{s,i})$ is the conditional probability matrix where $\phi_{s,i}$ is measured to be $\phi_{s,j}$, and $\varepsilon_i = \sum_j P(\phi_{s,j}|\phi_{s,i})$ is the efficiency. In the iterative calculation, $\hat{n}(\Delta\phi, \phi_s)$ also serves as the prior distribution of the next loop. We perform this unfolding separately for every $\Delta\phi$ bin.

We define the experimentally observed distribution as $n^{\rm obs}(\Delta\phi, \phi_s) = 1 + Y(\Delta\phi, \phi_s)$ by using the measured event-plane-dependent per-trigger yield. The offset is to prevent a divergence in the iteration due to small yields near the ZYAM point. In the initial loop of the iteration, we define the prior distribution as $n(\Delta\phi, \phi_s) = n^{\rm obs}(\Delta\phi, \phi_s)$.

The probability distribution of the relative azimuthal angle between the true event plane Ψ_n and the measured event plane $\Psi_n^{\rm obs}$ can be translated into the difference between real and observed ϕ_s as

$$\Psi_n - \Psi_n^{\rm obs} = \left(\phi^t - \Psi_n^{\rm obs}\right) - (\phi^t - \Psi_n) = \phi_s^{\rm obs} - \phi_s. \tag{27}$$

With this probability distribution of $\phi_s^{\rm obs} - \phi_s$, the probability matrix $P(\phi_{s,j}|\phi_{s,i})$ is determined by the degree of the

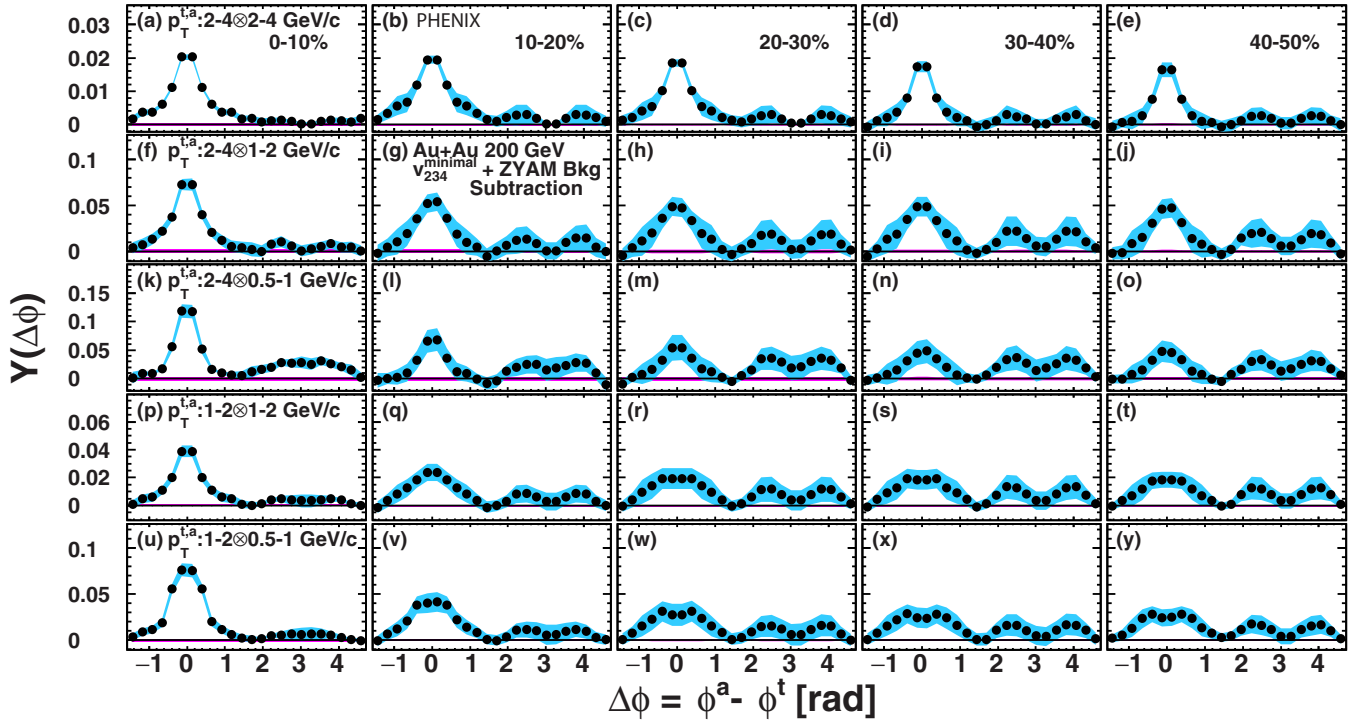

FIG. 15. Per-trigger yields $Y(\Delta\phi)$ of dihadron pairs measured in Au + Au collisions after subtracting the underlying event model with several p_T selections of the trigger and associated particles ($p_T^{t,a}$): (a)–(e) $(2 < p_T^t < 4) \otimes (2 < p_T^a < 4)$ GeV/c, (f)–(j) $(2 < p_T^t < 4) \otimes (1 < p_T^a < 2)$ GeV/c, (k)–(o) $(2 < p_T^t < 4) \otimes (0.5 < p_T^a < 1)$ GeV/c, (p)–(t) $(1 < p_T^t < 2) \otimes (1 < p_T^a < 2)$ GeV/c, and (u)–(y) $(1 < p_T^t < 2) \otimes (0.5 < p_T^a < 1)$ GeV/c. The columns represent centrality bins (a), (f), (k), (p), (u) 0%–10%; (b), (g), (l), (q), (v) 10%–20%, (c), (h), (m), (r), (w) 20%–30%, (d), (i), (n), (s), (x) 30%–40%, and (e), (j), (o), (t), (y) 40%–50%. Systematic uncertainties are shown by (blue) bands around the points. Uncertainties from ZYAM are shown by (purple) bands around zero yield.

contamination by neighboring ϕ_s bin as

$$P(\phi_{s,j}|\phi_{s,i}) = \begin{pmatrix} s_0 & s_1 & s_2 & s_3 & s_4 & s_5 & s_6 & s_7 \\ s_7 & s_0 & s_1 & s_2 & s_3 & s_4 & s_5 & s_6 \\ s_6 & s_7 & s_0 & s_1 & s_2 & s_3 & s_4 & s_5 \\ s_5 & s_6 & s_7 & s_0 & s_1 & s_2 & s_3 & s_4 \\ s_4 & s_5 & s_6 & s_7 & s_0 & s_1 & s_2 & s_3 \\ s_3 & s_4 & s_5 & s_6 & s_7 & s_0 & s_1 & s_2 \\ s_2 & s_3 & s_4 & s_5 & s_6 & s_7 & s_0 & s_1 \\ s_1 & s_2 & s_3 & s_4 & s_5 & s_6 & s_7 & s_0 \end{pmatrix}, \quad (28)$$

where s_n ($n \neq 0$) is the contamination fraction from the nth ϕ_s bin away from a selected ϕ_s bin, and s_0 is the fraction of the true signal in the selected ϕ_s bin. A study in previous identified particle v_2 measurements of the PHENIX experiment [68] using the same data sample as this analysis showed that the tracking efficiency is independent of ϕ_s. Thus, we normalize the probability as $\sum s_n = 1$, i.e., $\varepsilon = 1$. Due to the cyclic boundary condition in the azimuthal angle direction, symmetric elements of $P(\phi_{s,j}|\phi_{s,i})$ are identical i.e., $s_5 = s_3$, $s_6 = s_2$, and $s_7 = s_1$. The matrix $P(\phi_{s,j}|\phi_{s,i})$ depends only on the order of event planes and centrality. An example of corrections based on this iterative method at $-\frac{\pi}{24} < \Delta\phi < 0$ for $(2 < p_T^t < 4) \otimes (1 < p_T^a < 2)$ GeV/c in 20%–30% central collisions is shown in Fig. 11 together with an example of the Fourier analysis method introduced in Sec. III D 2.

2. *Fourier oscillation correction of event-plane-dependence of correlations*

The second method to correct the event-plane-dependence of the per-trigger yield is a Fourier analysis. $Y(\Delta\phi, \phi_s)$ is offset by 1 to prevent divergences in the correction due to small values due to the ZYAM subtraction of the background. A Fourier series should be able to fit the event-plane dependence of $1 + Y(\Delta\phi, \phi_s)$, and the fit function to the Ψ_2-dependent case at a given $\Delta\phi$ can be written as

$$F^Y(\Delta\phi, \phi_s) = a_0\left[1 + \sum_{n=2,4} 2a_n \cos n(\phi_s + \Delta\phi)\right], \quad (29)$$

and similarly the Ψ_3-dependent case can be written as

$$F^Y(\Delta\phi, \phi_s) = a_0[1 + 2a_3 \cos 3(\phi_s + \Delta\phi)], \quad (30)$$

where a_0 is a normalization and a_2, a_3, and a_4 are the azimuthal anisotropies of $1 + Y(\Delta\phi, \phi_s)$. In the fitting functions $F^Y(\Delta\phi, \phi_s)$, the phase shift $\Delta\phi$ is necessary in $1 + Y(\Delta\phi, \phi_s)$ because the associated yields are at $\phi^a - \Psi_n = \phi_s + \Delta\phi$ (see Fig. 2).

With the assumption that the coefficients determined from the fits are diluted by the event-plane resolutions, the effects can be corrected in a manner analogous to the single-particle azimuthal anisotropy v_n as performed in Ref. [16]. For the

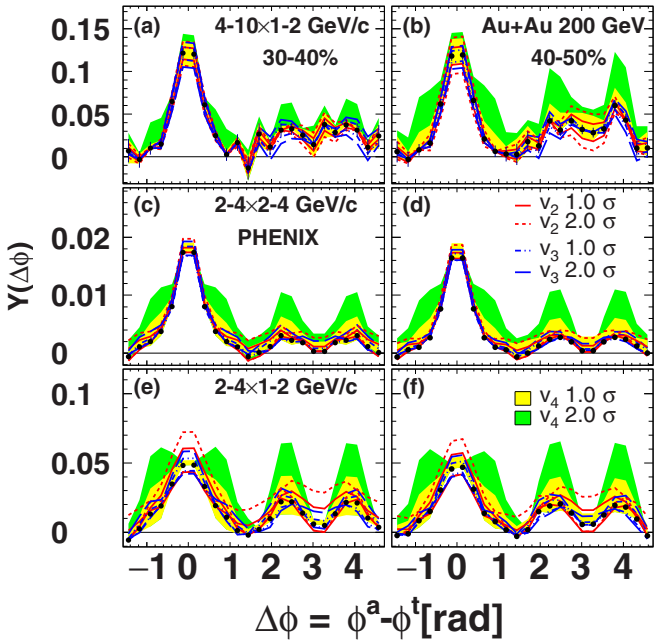

FIG. 16. Per-trigger yields $Y(\Delta\phi)$ of dihadron pairs measured in Au + Au collisions after subtracting the underlying event-model with several p_T selections: (a)–(b) $(4 < p_T^t < 10) \otimes (1 < p_T^a < 2)$ GeV/c, (c)–(d) $(2 < p_T^t < 4) \otimes (2 < p_T^a < 4)$ GeV/c, and (e)–(f) $(2 < p_T^t < 4) \otimes (1 < p_T^a < 2)$ GeV/c. The columns represent centrality bins (a), (c), (e) 30%–40% and (b), (d), (f) 40%–50%. The lines and bands further break down of the uncertainty contributions from each different order of the v_n subtraction. The systematic uncertainties are point-to-point correlated. If the yield at $\Delta\phi = \pi$ is reduced, the away-side yield outside the region $\Delta\phi = \pi$ is increased.

Ψ_2-dependent case, the correction is given as

$$F^{Y,\mathrm{cor}}(\Delta\phi, \phi_s) = a_0\left[1 + \sum_{n=2,4} \frac{2a_n \cos n(\phi_s + \Delta\phi)}{\mathrm{Res}\{n, \Psi_2\}}\right], \quad (31)$$

and for the Ψ_3-dependent case it is given as

$$F^{Y,\mathrm{cor}}(\Delta\phi, \phi_s) = a_0\left[1 + \frac{2a_3 \cos 3(\phi_s + \Delta\phi)}{\mathrm{Res}\{3, \Psi_3\}}\right]. \quad (32)$$

The correction coefficient to $1 + Y^{\mathrm{cor}}$ is then given by the ratio $F^{Y,\mathrm{cor}}(\phi_s)/F^Y(\phi_s)$, which then fixes the corrected per-trigger yield as

$$1 + Y^{\mathrm{cor}}(\Delta\phi, \phi_s) = \frac{F^{Y,\mathrm{cor}}(\Delta\phi, \phi_s)}{F^Y(\Delta\phi, \phi_s)}[1 + Y(\Delta\phi, \phi_s)]. \quad (33)$$

E. Systematic uncertainties for per-trigger yields

1. Efficiency

Systematic uncertainties in tracking efficiency are estimated to be approximately 10% for $p_T < 4$ GeV/c and 13% for $p_T > 4$ GeV/c independent of centrality [7,16,28,47].

2. Inclusive per-trigger yields

Systematic uncertainties on the yields from the matching cut and from the v_n measurements are determined by the variations on the parameters discussed below. The systematic uncertainty from the matching cut σ_{mat} after flow subtraction is derived in a similar manner as in previous publications [47]:

$$\sigma_{\mathrm{mat}} = |Y^{\mathrm{mat}=2.5\sigma}(\Delta\phi) - Y^{\mathrm{mat}=1.5\sigma}(\Delta\phi)|/2. \quad (34)$$

The systematic uncertainties from v_n are evaluated by taking the quadrature sum of residuals from the 1-σ uncertainties on the v_n for all orders of n used in the subtraction. Formally, the calculation is given by

$$\sigma_v = \sqrt{\sum_{k=2,3,4}\sum_{l=\pm1} \frac{\left|Y^{v_k^{l\sigma}}(\Delta\phi) - Y^{v_k}(\Delta\phi)\right|^2}{2}}, \quad (35)$$

where the second $Y(\Delta\phi)$ refers to the yields resulting from the default set of measured v_n values. The total systematic uncertainties σ_{in} in the inclusive trigger yields are given by

$$\sigma_{\mathrm{in}} = \sqrt{\sigma_v^2 + \sigma_{\mathrm{mat}}^2}. \quad (36)$$

We studied the inclusion of a v_5 term assuming $v_5 = 0.5v_4$, consistent with the ATLAS measurements [34]. The results were completely consistent with the quoted uncertainties. Uncertainties due to ZYAM will be discussed later.

3. Event-plane-dependent per-trigger yields

In addition to systematic uncertainties considered in the inclusive per-trigger yields, systematic uncertainties due to the $\cos 4(\Psi_4 - \Psi_2)$ correlation strength are also taken into account before the unfolding of event-plane resolution effects. The value of χ_{42} is determined from $v_4\{\Psi_4\}$ and $v_4\{\Psi_2\}$, and the systematic uncertainties of χ_{42} are propagated from those of $v_4\{\Psi_2\}$. Systematic uncertainties in the yield due to χ_{42} are given by

$$\sigma_{\chi_{42}} = \sqrt{\sum_{l=\pm1} \frac{\left|Y^{\chi_{42}^{l\sigma}}(\Delta\phi, \phi_s) - Y^{\chi_{42}}(\Delta\phi, \phi_s)\right|^2}{2}}. \quad (37)$$

The systematic uncertainties before unfolding are

$$\sigma_{\mathrm{bef}} = \sqrt{\sigma_v^2 + \sigma_{\mathrm{mat}}^2 + \sigma_{\chi_{42}}^2}. \quad (38)$$

For the event-plane-dependent per-trigger yields, the systematic uncertainty due to the impact of the finite event-plane resolution on the correlations has contributions from the method and the number of iterations in the Bayesian method. The uncertainty due to the method is given by

$$\sigma_{\mathrm{Met}} = \left|Y_{\mathrm{unf}}^{\mathrm{fit}} - Y_{\mathrm{unf}}^{\mathrm{itr}}\right|, \quad (39)$$

where $Y_{\mathrm{unf}}^{\mathrm{itr}}$ is the result using the iterative Bayesian method and $Y_{\mathrm{unf}}^{\mathrm{fit}}$ is the result of using the Fourier fitting method. The uncertainty due to the number of interactions using for unfolding is given by the difference between the number of iterations (Nit) for $n = 5$ and $n = 10$:

$$\sigma_{\mathrm{Nit}} = \left|Y_{\mathrm{unf}}^{n=5} - Y_{\mathrm{unf}}^{n=10}\right|. \quad (40)$$

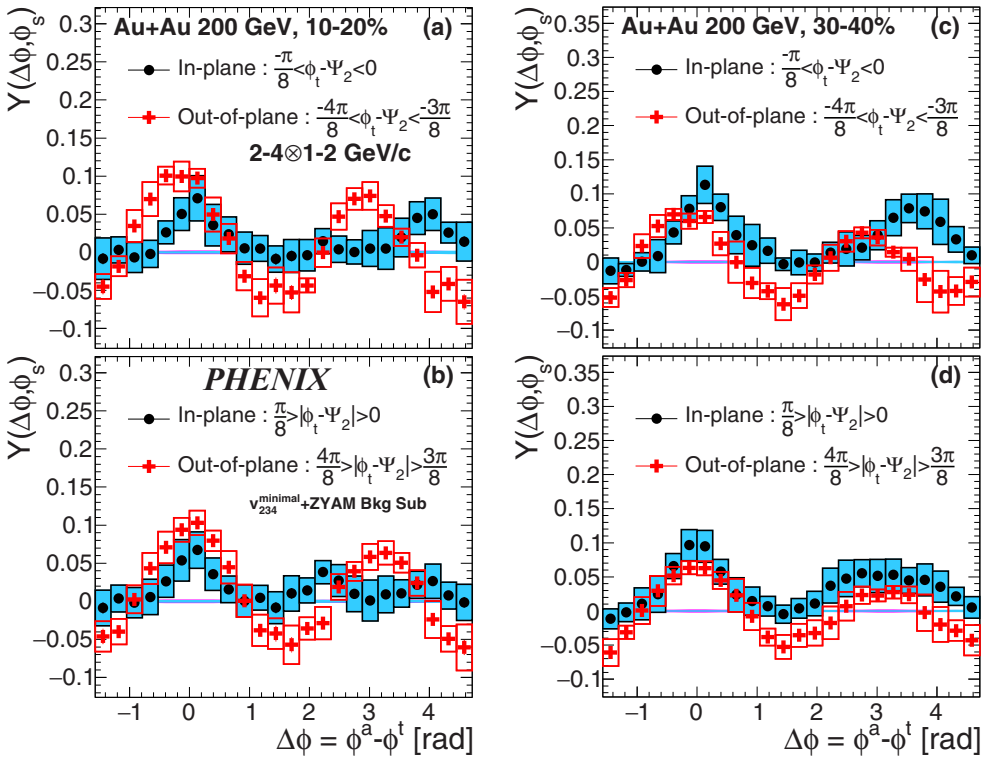

FIG. 17. Ψ_2 event-plane-dependent per-trigger yields $Y(\Delta\phi)$ of dihadron pairs measured in Au + Au collisions after subtracting the underlying event model for $(2 < p_T^t < 4) \otimes (1 < p_T^a < 2)$ GeV/c and (a), (b) 10%–20% and (c), (d) 30%–40%. In-plane $0 < |\phi^t - \Psi_2| < \pi/8$ are (black) circles and out-of-plane $3\pi/8 < |\phi^t - \Psi_2| < 4\pi/8$ are (red) crosses. The sign of $\phi^t - \Psi_2$ is negative in panels (a) and (c) and both positive and negative in panels (b) and (d). The ZYAM systematic uncertainties are shown in the band around zero yield. The other systematic uncertainties are shown in the boxes around the points.

These unfolding uncertainties are added in quadrature to the uncertainties before unfolding

$$\sigma_{\rm tot} = \sqrt{\sigma_{\rm bef}{}^2 + \sigma_{\rm Met}{}^2 + \sigma_{\rm Nit}{}^2}. \tag{41}$$

In event-plane-dependent per-trigger yields, we also unfolded the upper and lower boundaries of ZYAM uncertainties propagated from statistical uncertainties from the data. The systematic uncertainties associated with ZYAM are not included into the total systematic uncertainties $\sigma_{\rm tot}$. These variations are discussed below.

IV. RESULTS AND DISCUSSION

A. Inclusive per-trigger yields I: High-p_T trigger particles

We first present the highest trigger p_T correlations. The jet-like correlations should be dominated by $2 \to 2$ scattering. Pairs of particles with $\Delta\phi = 0$, the near side, are from both particles fragmenting from a single jet. Pairs of hadrons around $\Delta\phi = \pi$, the away side, occur when each particle fragments from back-to-back jets. In high-p_T correlations the jet momentum fraction for the associated particle is approximated by

$$z_T = p_T^a/p_T^t. \tag{42}$$

Per-trigger yields with trigger particles from $4 < p_T^t < 10$ GeV/c paired with associated particles from $0.5 < p_T^a < 10$ GeV/c are shown in Fig. 12. The band around zero indicates the systematic uncertainty due the ZYAM assumption. The band around the data points is the systematic uncertainty from all other sources. Systematic uncertainties from the associated tracking efficiency and matching and the ZYAM normalization are fully correlated point to point. The underlying event subtraction is correlated point to point and can affect the shape. For the highest trigger p_T correlations, the dominant systematic is not the underlying event subtraction.

The near-side yield is centrality independent (Fig. 12). This is consistent with measurements of the two-particle correlation that indicated the near-side yields are not modified [21,27,30,45]. The lack of centrality dependence is also consistent with the picture that triggering on high-p_T particles biases the origin of the hard-scattering toward the surface of the QGP such that the leading parton loses little to no energy.

The away-side peak is evident in several p_T^a and centrality selections. The evolution of the away shape and yield with centrality and p_T^a is similar to previous measurements where only v_2 is assumed to contribute to the underlying event [29,46,47]. The away-side peak becomes sharper and more pronounced as p_T^a increases or the centrality selection becomes more peripheral. In more central collisions and lower p_T^a when the away-side structure is present, it is broader than in the highest p_T^a and peripheral centrality selection. The trends are consistent with a picture where the associated parton opposite the trigger loses energy and scatters in the medium.

At the lowest p_T^a a very wide plateau-like away-side structure is observed with similar shape and magnitude in all centralities. Similar low-momentum and large-angle yields have been observed in prior measurements [20,23–25].

Figure 13 shows the comparison between the highest-p_T^t correlations for each centrality with the same distributions measured in $p+p$ collisions from a previous analysis [47]. In that paper the lowest p_T^a bin was 0.4–1.0 GeV/c compared with 0.5–1.0 GeV/c in this analysis. Therefore, the lowest p_T^a bin from $p+p$ was modified by a $\Delta\phi$-dependent correction determined from PYTHIA 6 [79]. The correction, which has negligible uncertainties compared with those from other sources, was determined from the ratio of fits to the PYTHIA dihadron $\Delta\phi$ per-trigger yield distributions with $0.5 < p_T^a < 1.0$ GeV/c and $0.4 < p_T^a < 1.0$ GeV/c.

Previous correlation analyses that relied on v_2-only subtraction indicated that the near-side yield was enhanced in Au + Au compared with $p+p$, the so-called "ridge" [45,47]. Our updated underlying event model has reduced the near-side yield as expected [32]. In fact, the yields are slightly suppressed relative to $p+p$. The integrated away-side yields show modification relative to $p+p$. Figures 13(b) and 13(d) show the comparisons of the per-trigger yields for the lowest p_T^a. The away-side shapes of the Au + Au distributions are different from $p+p$. The large-angle enhancement of the per-trigger yield at low associated particle momentum is qualitatively consistent with measurements of direct photon-hadron and jet-hadron correlations with fully reconstructed jets [20,23–25].

To explore these features quantitatively, we calculate the ratio I_{AA} of the away-side yields in Au + Au to those in $p+p$:

$$I_{AA} = \frac{Y_{\mathrm{Au+Au}}(\Delta\phi)}{Y_{p+p}(\Delta\phi)}. \tag{43}$$

Figure 14(b) shows I_{AA} vs centrality when integrating the away side $0 < |\Delta\phi - \pi| < \pi/2$ for 4–10 GeV/c hadrons paired with 0.5–1.0 GeV/c hadrons. I_{AA} is unity within uncertainties indicating that yield suppression is disfavored. Figure 14(a) shows I_{AA} for two different angular regions of integration and p_T^a selections. First, for p_T^a from 4–10 GeV/c (high z_T) and integrating $0 < |\Delta\phi - \pi| < \pi/4$, the jet peak region, I_{AA} is less than unity, indicating that the pair yields are suppressed relative to those in $p+p$. This is consistent with previous measurements of strong suppression of high p_T^a [20,28]. When integrating $\pi/4 < |\Delta\phi - \pi| < \pi/2$ for p_T^a from 0.5–1.0 GeV/c (low z_T), $I_{AA} \sim 1$ within systematic uncertainties. This would indicate that the yield in Au + Au is similar to $p+p$. However, it is more instructive to compare the I_{AA} for a fixed p_T^t, which approximately fixes the jet energy. Figure 14(a) shows that the low-z_T fragments at large angles from $\Delta\phi = \pi$ are significantly enhanced compared with the suppressed level of high-z_T fragments within the jet region. Both the high-z_T suppression relative to $p+p$ and the enhanced level of low-z_T fragments at large angles are consistent with a radiative energy-loss model where the away-side jet traverses the medium, loses energy, and the energy gets redistributed to larger angles.

B. Inclusive per-trigger yields II: Intermediate-p_T trigger particles

Given the success of reproducing prior correlation results at high p_T^t, we study lower p_T^t correlations to attempt to measure jet-like correlations at lower momentum transfer Q^2. Per-trigger yields with trigger particles of $1 < p_T^t < 2$ and $2 < p_T^t < 4$ GeV/c paired with associated particles of 0.5 GeV/$c < p_T^a < p_T^t$ in several centrality selections are shown in Fig. 15. As in Fig. 12, the ZYAM uncertainties are shown as a band around zero while v_n uncertainties are combined as the band around the data points. At these p_T^t the jet-like signal-to-underlying-event background is reduced, making the contribution of the v_n uncertainties dominant. Because the v_n uncertainties are point-to-point correlated, it is important to recognize that the yields and shape change due to that correlation. For example, if the v_2 subtracted is too large, the effect on the away side is a reduced peak and

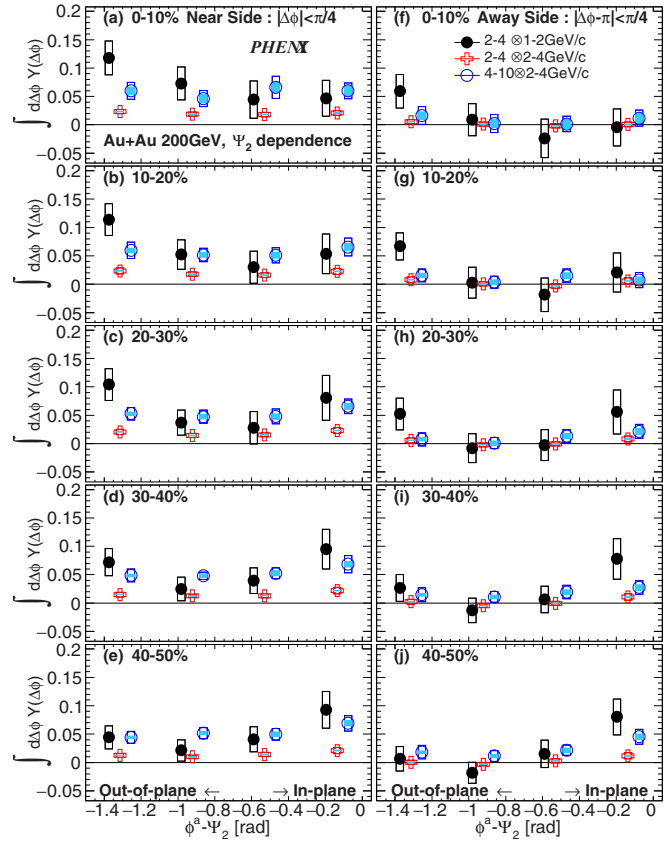

FIG. 18. Integrated per-trigger yields as a function of associated particle angle relative to Ψ_2 event plane $\phi^a - \Psi_2$ integrated (a)–(e) over the near side $|\Delta\phi| < \pi/4$ and (f)–(j) over the away side $|\Delta\phi - \pi| < \pi/4$. The columns represent centrality bins (a), (f) 0%–10%; (b), (g) 10%–20%; (c), (h) 20%–30%; (d), (i) 30%–40%; and (e), (j) 40%–50%. The ranges of $p_T^t \otimes p_T^a$ are (filled black circles) $(2 < p_T^t < 4) \otimes (1 < p_T^a < 2)$ GeV/c, (open red squares), $2 < p_T^t < 4 \otimes (2 < p_T^a < 4)$ GeV/c, and (open blue circles) $(4 < p_T^t < 10) \otimes (2 < p_T^a < 4)$ GeV/c. The ZYAM systematic uncertainties are shown in the solid light-blue boxes around the data points. The other systematic uncertainties are shown in the open boxes around the points.

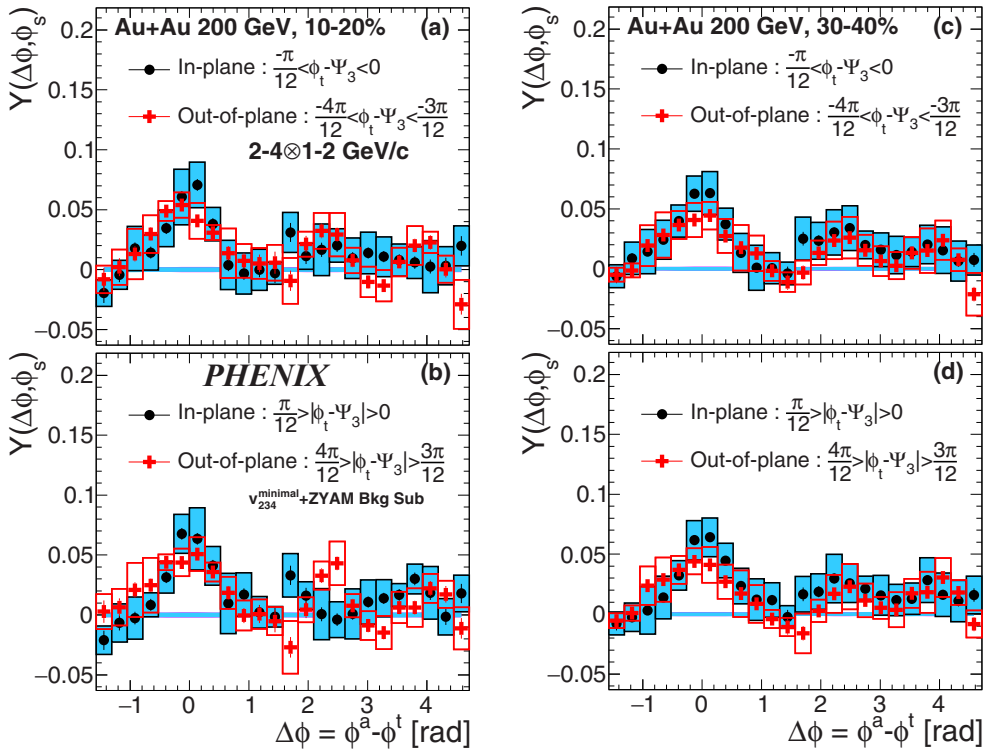

FIG. 19. Ψ_3 event-plane-dependent per-trigger yields $Y(\Delta\phi)$ of dihadron pairs measured in Au + Au collisions after subtracting the underlying event model for $(2 < p_T^t < 4) \otimes (1 < p_T^a < 2)$ GeV/c and (a), (b) 10%–20% and (c), (d) 30%–40%. In-plane $0 < |\phi^t - \Psi_3| < \pi/12$ are (black) circles and out-of-plane $3\pi/12 < |\phi^t - \Psi_3| < 4\pi/12$ are (red) crosses. The sign of $\phi^t - \Psi_3$ is negative in panels (a) and (c) and both positive and negative in panels (b) and (d). The ZYAM systematic uncertainties are shown in the band around zero yield. The other systematic uncertainties are shown in the boxes around the points.

an enhanced large-angle yield. If the v_2 subtracted is too small, the away-side becomes more peaked. In the discussion that follows we only make statements that have a significant variation over the systematic uncertainties.

The away-side yield and shape varies with both p_T^a and centrality. In these p_T selections and in the most-central collisions, the away-side seems to completely disappear. If our background model represents all nonjet correlations, the disappearance is presumably due to jet quenching. Compared to v_2-only subtraction [47], the very large displaced away-side peaks are reduced primarily due to the subtraction of v_3 in the underlying event [32]. Both the flat away-side and the near-side peak shape seem relatively centrality independent.

To better assess the systematic significance of the correlation features at the lower p_T^a selections, Fig. 16 shows a further breakdown of the uncertainty contributions from different orders of the v_n subtraction. The lines and bands show the 1σ and 2σ variation of each of the v_n components independently. Here the ZYAM level is recalculated for every v_n variation. These uncertainties are point-to-point correlated where a reduction at $\Delta\phi = \pi$ leads to an increase at angles away from π. The v_4 dominates the uncertainty in the away-side shape. The location of any double-peak structure in the away-side is also strongly dependent on the underlying event background subtraction. The peak in the uncertainties from v_2, v_3, and v_4 are all at slightly different places. Therefore, a robust and well-motivated background model is necessary to extract detailed shape information at these p_T^a. With our quoted systematic uncertainties, we cannot distinguish between a single broad away-side peak structure or a double-hump structure.

C. Event-plane-dependent correlations

Figure 17 shows Ψ_2-dependent per-trigger yields of trigger particles from $2 < p_T^t < 4$ GeV/c with associated particles from $1 < p_T^a < 2$ GeV/c in 10%–20% and 30%–40% central collisions. In Figs. 17(b) and 17(d), the trigger is selected to be either in-plane $0 < |\phi_s| < \pi/8$ or out-of-plane $3\pi/8 < |\phi_s| < \pi/2$, respectively. Similar to the inclusive per-trigger yields, we observe a broad away-side structure in both cases. The use of a common ZYAM point results in a slight over-subtraction in the out-of-plane bins. The over-subtraction can be corrected by determining a ZYAM point for each ϕ_s selection, which however makes event-plane-dependent correlations integrated over the ϕ_s bins different from inclusive correlations. This would result in moving all yield points up and does not affect the discussion of the shape that follows.

In Figs. 17(a) and 17(c), we chose the trigger to have a particular sign of ϕ_s. That is, we choose $-\pi/8 < \phi_s < 0$ and $-\pi/2 < \phi_s < -3\pi/8$ for the in-plane and out-of-plane, respectively. Choosing the sign of ϕ_s to be negative results in

always choosing the trigger to be "below" the event plane, if the event plane is the horizontal. When sign-selecting ϕ_s, an asymmetry around $\Delta\phi \sim 0$ and $\Delta\phi \sim \pi$ is observed. Such an asymmetry does not exist when choosing both signs of ϕ_s. In the in-plane-trigger case, there is a preference for the associated particle to be emitted toward the in-plane direction, i.e., the thinner side of the overlap region. Referring back to Fig. 1, our data suggest that Gluon 1 is more likely to be measured than Gluon 2. Other Ψ_2-dependent per-trigger yields with a selection of trigger azimuthal angle relative to event planes $\phi^t - \Psi_n < 0$ for different collision centralities and $p_T^{t,a}$ selections are shown in the Appendix.

The integrated per-trigger yields are shown in Fig. 18 as a function of associated particle angle with respect to Ψ_2. Figure 18 shows data for all centralities and all four orientations with respect to the event plane. We note that the use of a single ZYAM level for all event-plane bins can result in negative yields for certain $\Delta\phi$.

In Figs. 18(a)–18(e), the yields have been integrated for the near side $|\Delta\phi| =< \pi/4$. For all trigger and associated combinations there is weak to no dependence of the yield on event-plane orientation. This trend persists for all centrality selections.

In Figs. 18(f)–18(j), the yields have been integrated for the away side $|\Delta\phi - \pi| < \pi/4$. For the event-plane selections in the range $-1.2 < \phi^a - \Psi_2 < -0.5$, no significant yields are generally observed for both the highest- and lowest-trigger p_T. In the most-central collisions, for $(2 < p_T^t < 4) \otimes (1 < p_T^a < 2)$ GeV/c, the largest yield is out-of-plane. The difference between the in-plane and out-of-plane yields is approximately 1σ. This trend is opposite in the most-peripheral collision selection where the largest yield is in-plane. In 10%–40% central collisions, similar yields are observed in-plane versus out-of-plane. For $(2 < p_T^t < 4) \otimes (1 < p_T^a < 2)$ GeV/c, there is a possible trend with centrality that out-of-plane yield is reduced from central to peripheral collisions whereas in-plane yield increases from central to peripheral collisions. The significance of this possible trend is approximately 1σ.

Correlations selecting the trigger within a certain azimuthal angle from the Ψ_3 plane are shown in Fig. 19. The triangular shape of the third Fourier component restricts the range: $-\pi/3 < \Psi_3 \leqslant \pi/3$. The out-of-plane direction is at $\pm\pi/3$ radians relative to Ψ_3. In Figs. 19(b) and 19(d), we do not select the sign for ϕ_s. Similar to the inclusive distributions, there is a broad away-side structure that has a small yield. In Figs. 19(a) and 19(c), we select for $\phi_s < 0$. No discernible asymmetry is observed. It is possible that unfolding with the smaller Ψ_3 event-plane resolution could obscure any effect. Other Ψ_3-dependent per-trigger yields with a selection of trigger azimuthal angle relative to event planes $\phi^t - \Psi_n < 0$ for different collision centralities and $p_T^{t,a}$ selections are shown in the Appendix.

Similar to the Ψ_2-dependent correlations, we also integrate the per-trigger yields. This is shown in Fig. 20 for each centrality and associated particle azimuthal angle with respect to Ψ_3. Figures 20(a)–20(e) show the near-side integral. Figures 20(f)–20(j) show the away-side integral. In all cases, no event-plane-dependent or centrality-dependent trends are observed within uncertainties.

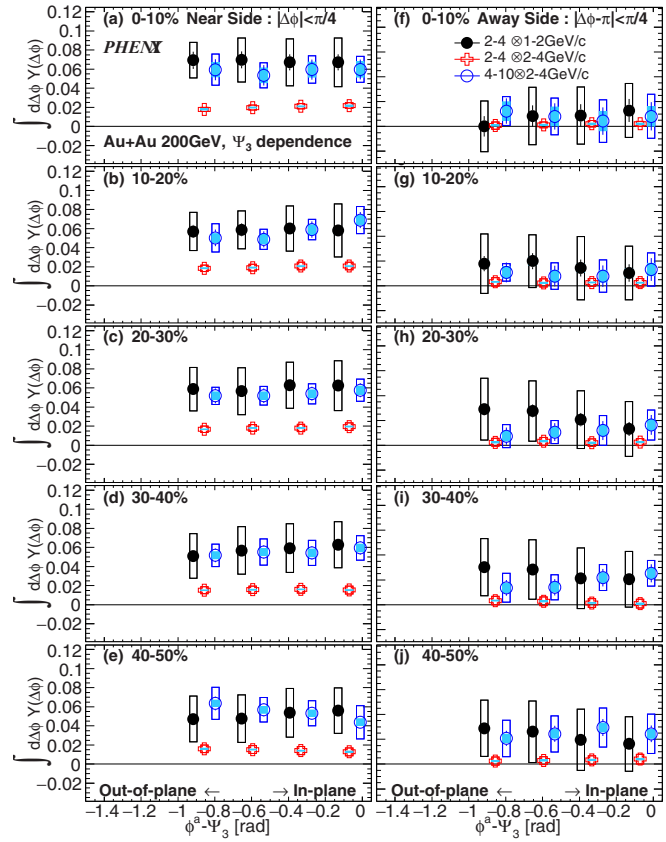

FIG. 20. Integrated per-trigger yields as a function of associated particle angle relative to Ψ_3 event plane for (a)–(e) near-side $|\Delta\phi| < \pi/4$ and (f)–(j) away-side $|\Delta\phi - \pi| < \pi/4$. The columns represent centrality bins 0%–10% (top), 10%–20%, 20%–30%, 30%–40%, 40%–50% (bottom). The ranges of $p_T^t \otimes p_T^a$ are $(2 < p_T^t < 4) \otimes (1 < p_T^a < 2)$ GeV/c (filled black circles), $2 < p_T^t < 4 \otimes 2 < p_T^a < 4$ GeV/c (red squares), and $(4 < p_T^t < 10) \otimes (2 < p_T^a < 4)$ GeV/c (open blue circles). The ZYAM systematic uncertainties are shown in the solid light-blue boxes around the data points. The other systematic uncertainties are shown in the open boxes around the points.

V. SUMMARY

In summary, we reported the two-particle azimuthal dihadron correlation measurements at $|\Delta\eta| < 0.7$ in Au + Au collisions at $\sqrt{s_{NN}} = 200$ GeV with and without subtraction of an underlying event. The underlying event model includes modulations from higher-order flow coefficients v_n $(n = 2, 3, 4)$ that assumes only the expected correlation of second- and fourth-order event planes.

We tested this two-source model by studying high-p_T(>4 GeV/c) triggers. We observe suppression of high-z_T jet fragments as well as enhancement of low-z_T jet fragments off the away-side jet axis. These results are consistent with previous dihadron and γ-hadron correlations and jet analyses [6–11].

At lower trigger $p_T 2 < p_T^t < 4$ GeV/c, the near-side distribution is not enhanced compared with $p + p$, which traditionally is associated with the ridge. When a significant away-side yield exists, the double-hump structure that had

been observed when subtracting a v_2-only underlying event is significantly reduced. Given our model assumptions and the systematic uncertainties on v_n, we cannot precisely determine if the away-side distribution is a single broadened peak or has further structure that may peak away from $\Delta\phi = \pi$.

We also present dihadron correlations selecting on ϕ_s, the angle of the trigger with respect to the event plane. When requiring ϕ_s to chose one side of the overlap region, the away-side developed an asymmetry in the $\Delta\phi$ distribution where the away-side yield is largest on the same side of the event plane. Such an asymmetry is qualitatively consistent with path-length-dependent energy loss where the away-side jet would have less medium to traverse when emerging from the same side of the overlap than being exactly back-to-back or through the opposite side. The observed asymmetry when the sign of the trigger with respect to the event plane is selected should set additional constraints on models of parton energy loss, and/or on models of the underlying event.

ACKNOWLEDGMENTS

We thank the staff of the Collider-Accelerator and Physics Departments at Brookhaven National Laboratory and the staff of the other PHENIX participating institutions for their vital contributions. We acknowledge support from the Office of Nuclear Physics in the Office of Science of the Department of Energy, the National Science Foundation, Abilene Christian University Research Council, Research Foundation of SUNY, and Dean of the College of Arts and Sciences, Vanderbilt University (USA), Ministry of Education, Culture, Sports, Science, and Technology and the Japan Society for the Promotion of Science (Japan), Conselho Nacional de Desenvolvimento Científico e Tecnológico and Fundação de Amparo à Pesquisa do Estado de São Paulo (Brazil), Natural Science Foundation of China (People's Republic of China), Croatian Science Foundation and Ministry of Science and Education (Croatia), Ministry of Education, Youth and Sports (Czech Republic), Centre National de la Recherche Scientifique, Commissariat à l'Énergie Atomique, and Institut National de Physique Nucléaire et de Physique des Particules (France), Bundesministerium für Bildung und Forschung, Deutscher Akademischer Austausch Dienst, and Alexander von Humboldt Stiftung (Germany), J. Bolyai Research Scholarship, EFOP, the New National Excellence Program (ÚNKP), NKFIH, and OTKA (Hungary), Department of Atomic Energy and Department of Science and Technology (India), Israel Science Foundation (Israel), Basic Science Research and SRC(CENuM) Programs through NRF funded by the Ministry of Education and the Ministry of Science and ICT (Korea); Physics Department, Lahore University of Management Sciences (Pakistan), Ministry of Education and Science, Russian Academy of Sciences, Federal Agency of Atomic Energy (Russia), VR and Wallenberg Foundation (Sweden), the U.S. Civilian Research and Development Foundation for the Independent States of the Former Soviet Union, the Hungarian American Enterprise Scholarship Fund, the US-Hungarian Fulbright Foundation, and the US-Israel Binational Science Foundation.

APPENDIX

Inclusive correlations before subtracting the underlying event model are shown in Figs. 21 and 22. Event-plane-dependent correlations and simulated-flow distributions are shown in Figs. 23–28. Event-plane-dependent per-trigger yields are shown in Figs. 29–34.

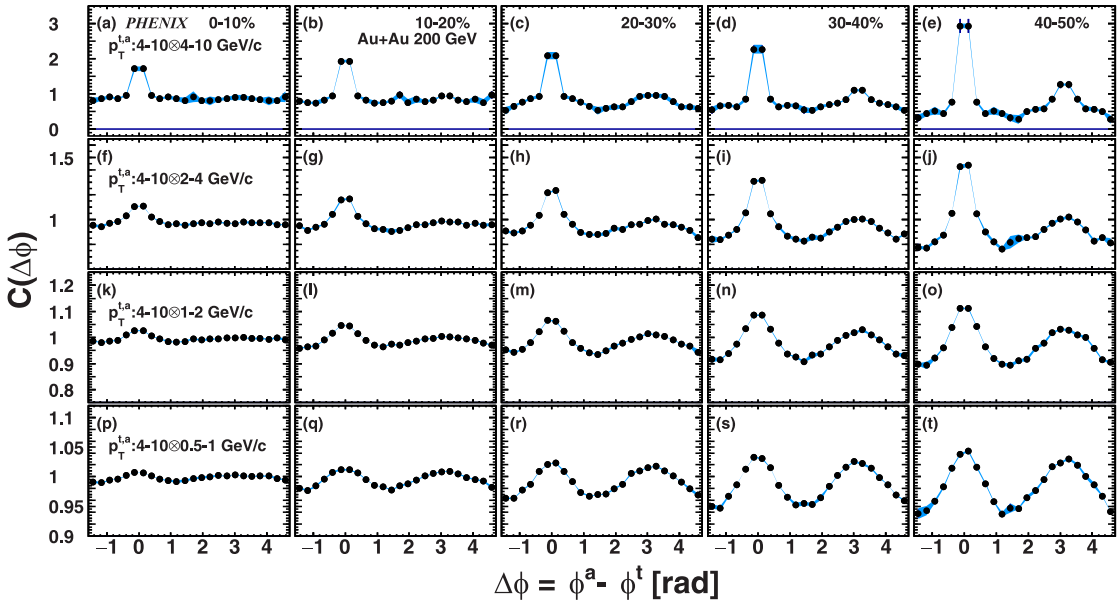

FIG. 21. Correlations $C(\Delta\phi)$ of dihadrons pairs measured in Au + Au collisions at $\sqrt{s_{NN}} = 200$ GeV before subtracting the underlying event model with several p_T selections: (a)–(e) $(4 < p_T^t < 10) \otimes (4 < p_T^a < 10)$ GeV/c, (f)–(j) $(4 < p_T^t < 10) \otimes (2 < p_T^a < 4)$ GeV/c, (k)–(o) $(4 < p_T^t < 10) \otimes (1 < p_T^a < 2)$ GeV/c, and (p)–(t) $(4 < p_T^t < 10) \otimes (0.5 < p_T^a < 1)$ GeV/c. The columns represent centrality bins (a), (f), (k), (p) 0%–10%; (b), (g), (l), (q) 10%–20%; (c), (h), (m), (r) 20%–30%; (d), (i), (n), (s) 30%–40%; and (e), (j), (o), (t) 40%–50%. Systematic uncertainties due to track matching are shown by blue bands around the points.

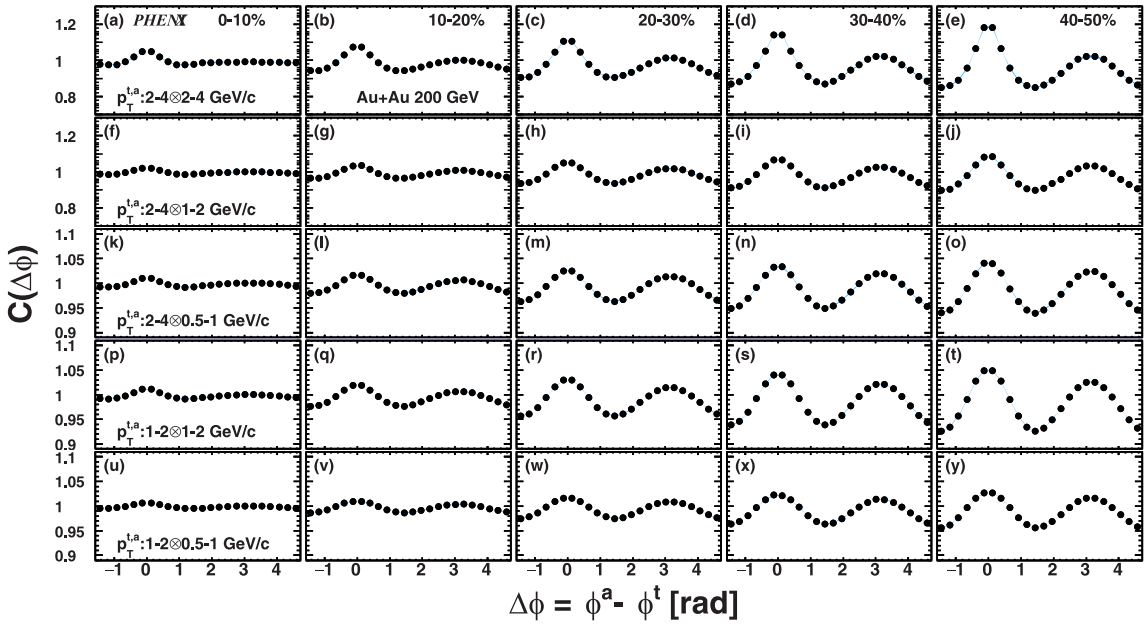

FIG. 22. Correlations $C(\Delta\phi)$ of dihadron pairs measured in Au + Au collisions before subtracting the underlying event model with several p_T selections of the trigger and associated particles ($p_T^{t,a}$): (a)–(e) $(2 < p_T^t < 4) \otimes (2 < p_T^a < 4)$ GeV/c, (f)–(j) $(2 < p_T^t < 4) \otimes (1 < p_T^a < 2)$ GeV/c, (k)–(o) $(2 < p_T^t < 4) \otimes (0.5 < p_T^a < 1)$ GeV/c, (p)–(t) $(1 < p_T^t < 2) \otimes (1 < p_T^a < 2)$ GeV/c, and (u)–(y) $(1 < p_T^t < 2) \otimes (0.5 < p_T^a < 1)$ GeV/c. The columns represent centrality bins (a), (f), (k), (p), (u) 0%–10%; (b), (g), (l), (q), (v) 10%–20%; (c), (d), (h), (i), (m), (n), (r), (s), (w), (x) 30%–40%; and (e), (j), (o), (t), (y) 40%–50%. Systematic uncertainties due to track matching are shown by blue bands around the points.

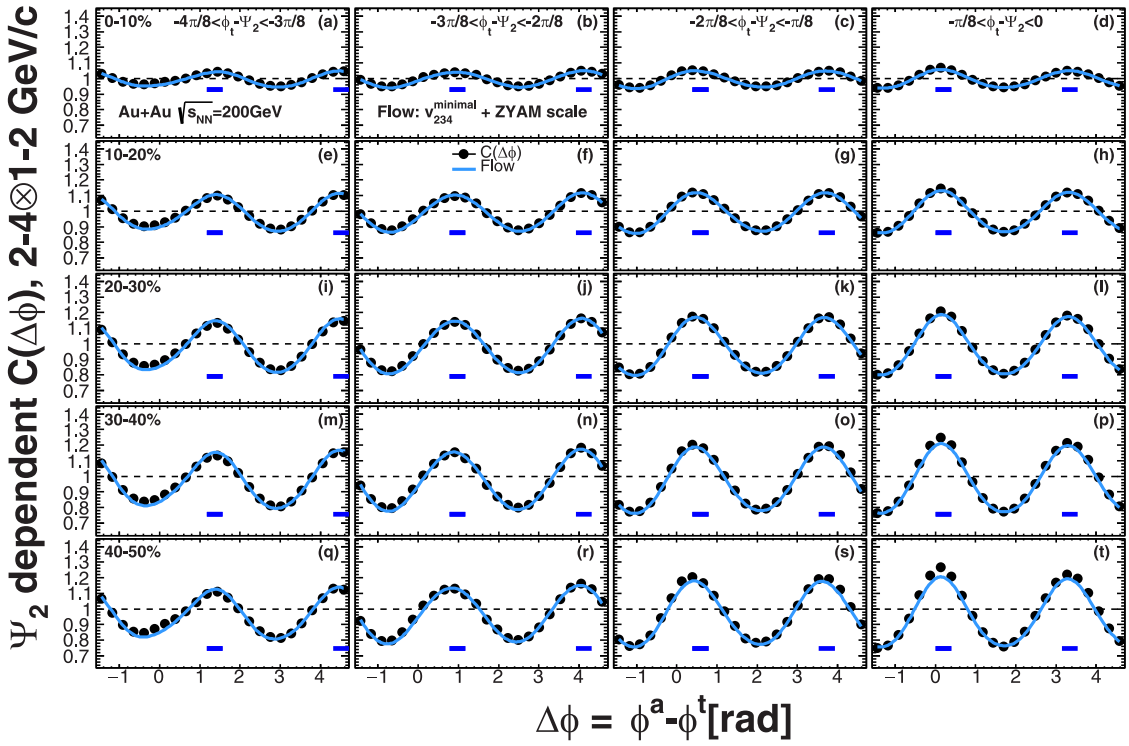

FIG. 23. Ψ_2-dependent correlations $C(\Delta\phi, \phi_s)$ and flow backgrounds $F(\Delta\phi, \phi_s)$ for $(2 < p_T^t < 4) \otimes (1 < p_T^a < 2)$ GeV/c. Trigger-particle azimuthal angle relative to the event plane $\phi_s = \phi^t - \Psi_2$ is selected out-of-plane (left) to in-plane (right). Centrality is 0%–10% (top) to 40%–50% (bottom).

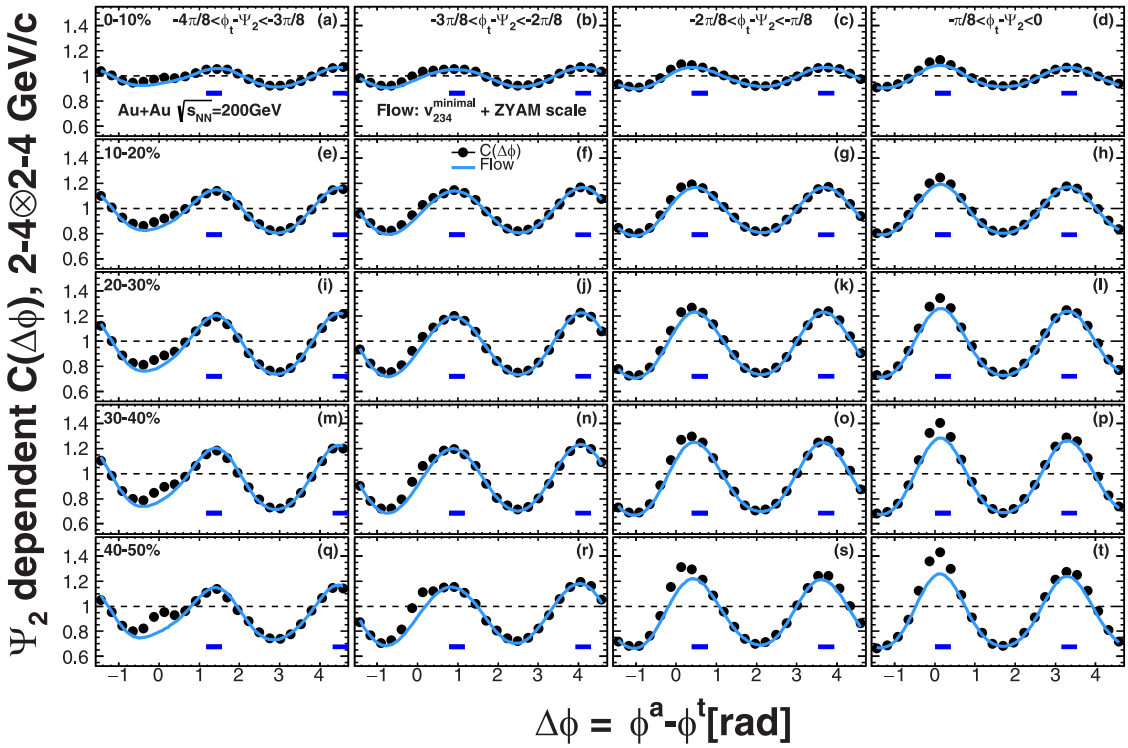

FIG. 24. Ψ_2-dependent correlations $C(\Delta\phi, \phi_s)$ and flow backgrounds $F(\Delta\phi, \phi_s)$ for $(2 < p_T^t < 4) \otimes (2 < p_T^a < 4)$ GeV/c. Trigger-particle azimuthal angle relative to the event plane $\phi_s = \phi^t - \Psi_2$ is selected out-of-plane (left) to in-plane (right). Centrality is 0%–10% (top) to 40%–50% (bottom).

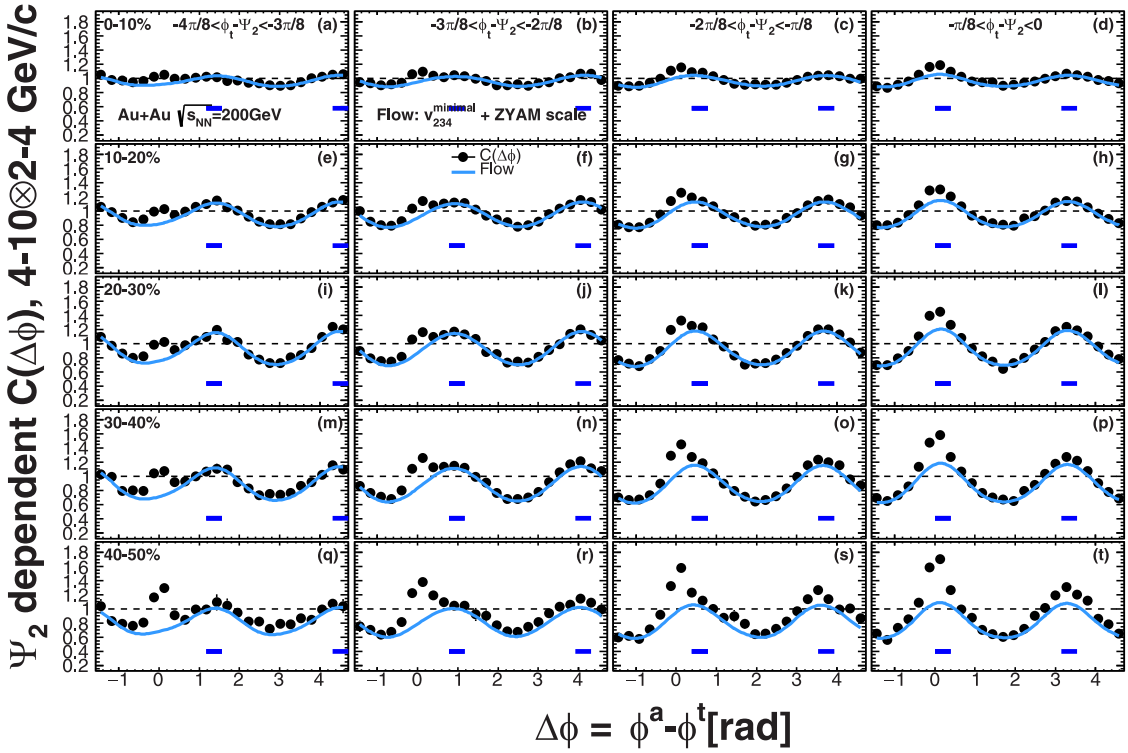

FIG. 25. Ψ_2-dependent correlations $C(\Delta\phi, \phi_s)$ and flow backgrounds $F(\Delta\phi, \phi_s)$ for $(4 < p_T^t < 10) \otimes (2 < p_T^a < 4)$ GeV/c. Trigger-particle azimuthal angle relative to the event plane $\phi_s = \phi^t - \Psi_2$ is selected out-of-plane (left) to in-plane (right). Centrality is 0%–10% (top) to 40%–50% (bottom).

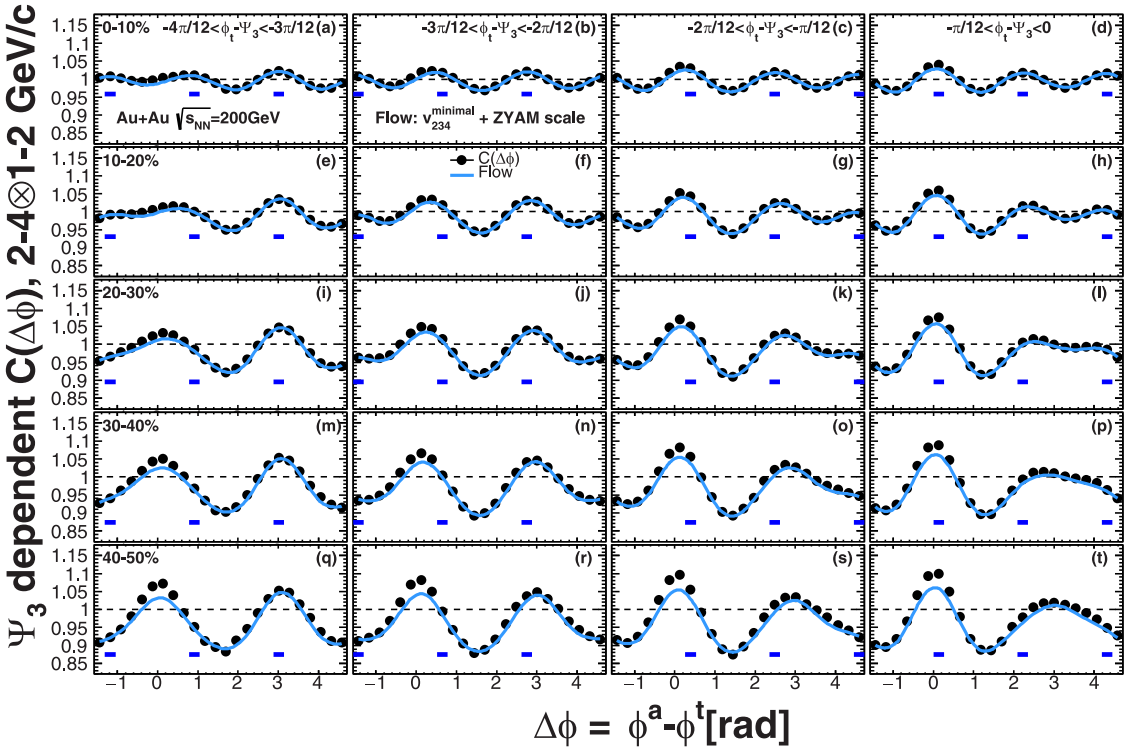

FIG. 26. Ψ_3-dependent correlations $C(\Delta\phi, \phi_s)$ and flow backgrounds $F(\Delta\phi, \phi_s)$ for $(2 < p_T^t < 4) \otimes (1 < p_T^a < 2)$ GeV/c. Trigger-particle azimuthal angle relative to the event plane $\phi_s = \phi^t - \Psi_3$ is selected out-of-plane (left) to in-plane (right). Centrality is 0%–10% (top) to 40%–50% (bottom).

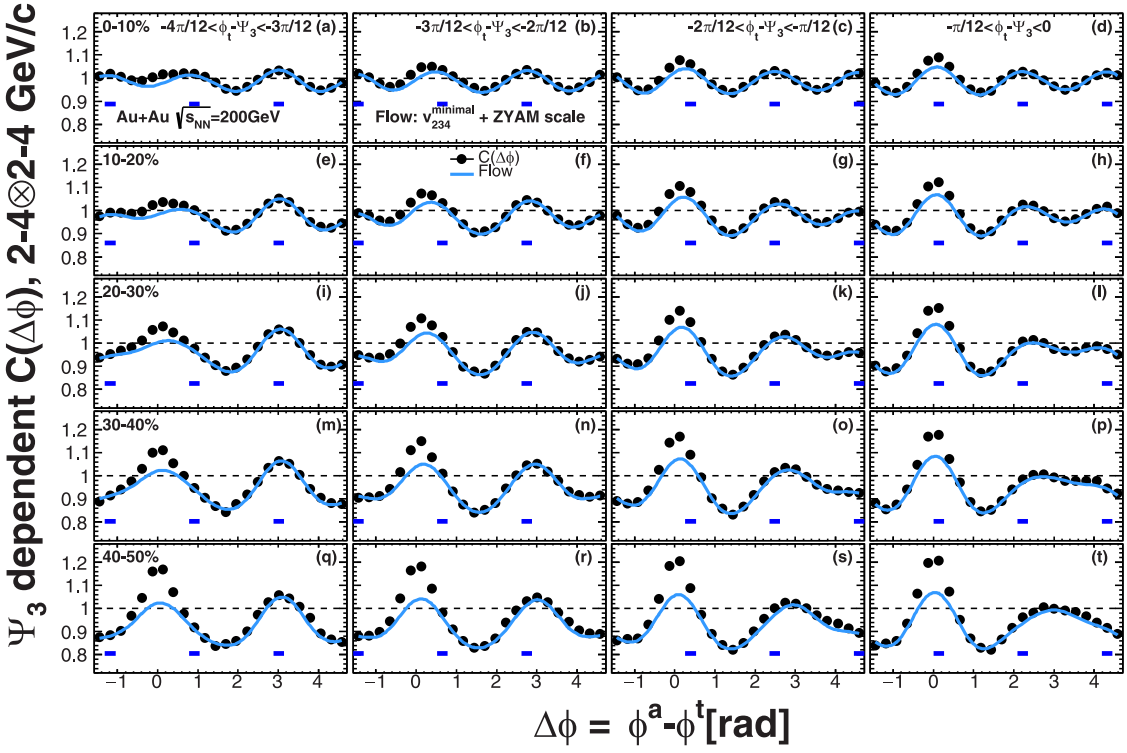

FIG. 27. Ψ_3-dependent correlations $C(\Delta\phi, \phi_s)$ and flow backgrounds $F(\Delta\phi, \phi_s)$ $(2 < p_T^t < 4) \otimes (2 < p_T^a < 4)$ GeV/c. Trigger-particle azimuthal angle relative to the event plane $\phi_s = \phi^t - \Psi_3$ is selected out-of-plane (left) to in-plane (right). Centrality is 0%–10% (top) to 40%–50% (bottom).

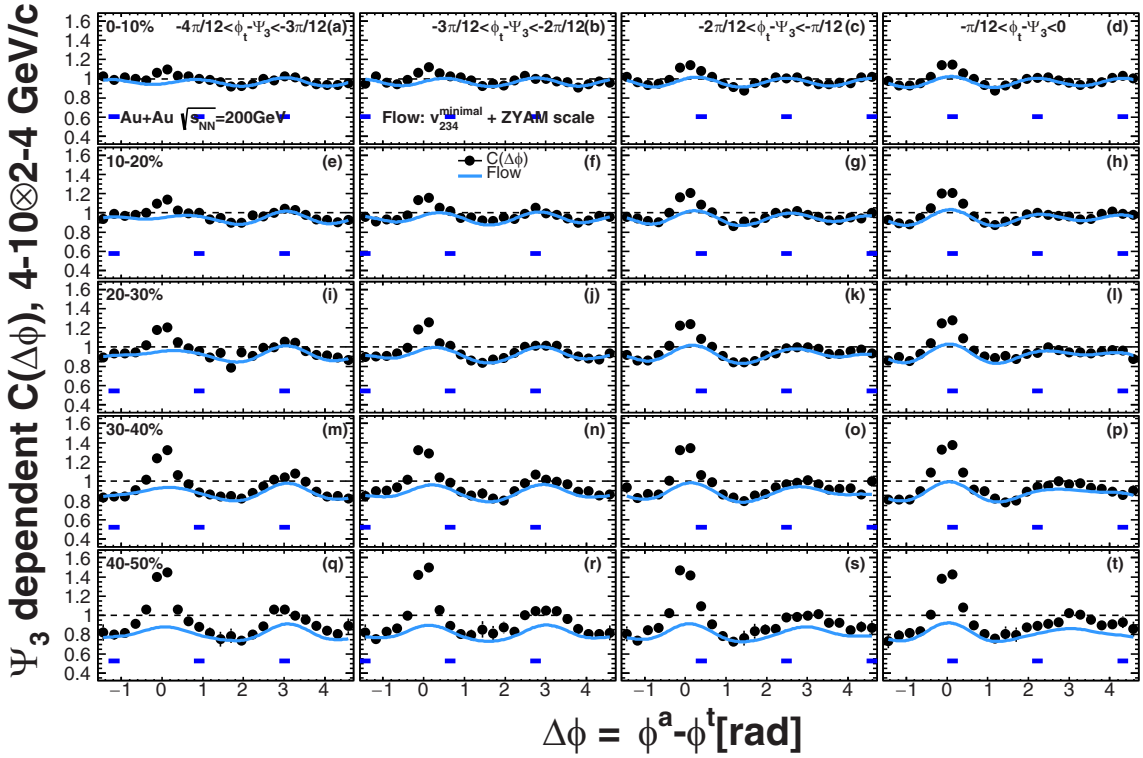

FIG. 28. Ψ_3-dependent correlations $C(\Delta\phi, \phi_s)$ and flow backgrounds $F(\Delta\phi, \phi_s)$ for $(4 < p_T^t < 10) \otimes (2 < p_T^a < 4)$ GeV/c. Trigger-particle azimuthal angle relative to the event plane $\phi_s = \phi^t - \Psi_3$ is selected out-of-plane (left) to in-plane (right). Centrality is 0%–10% (top) to 40%–50% (bottom).

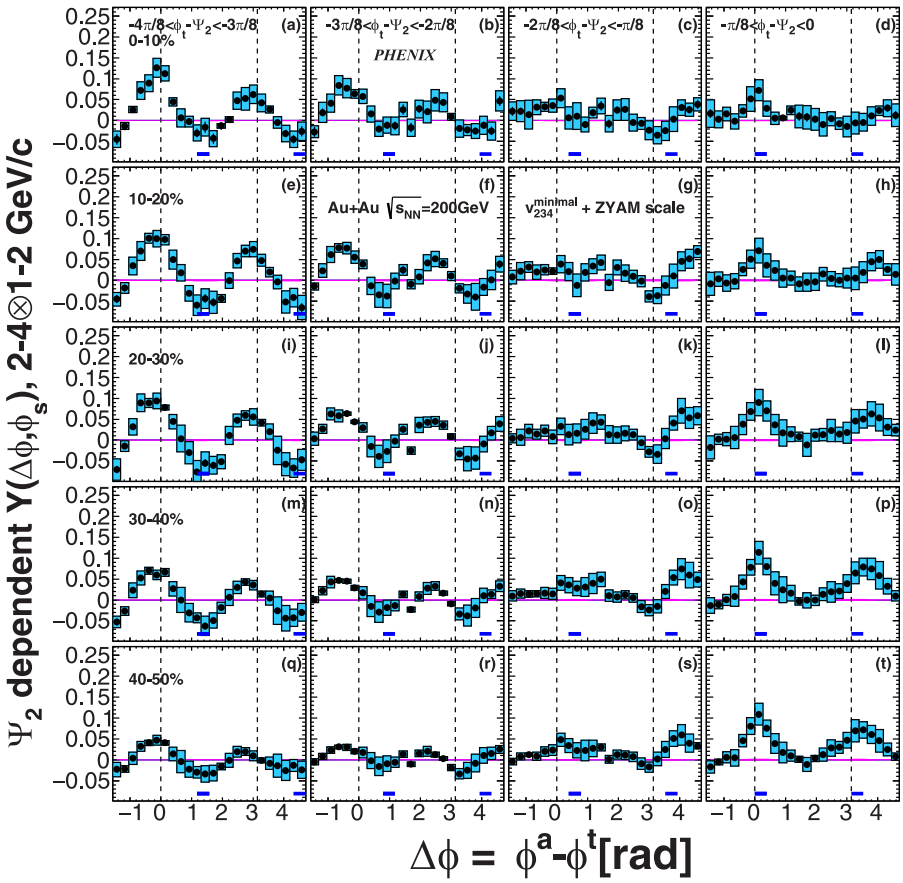

FIG. 29. Ψ_2-dependent per-trigger yields $Y(\Delta\phi, \phi_s)$ for $(2 < p_T^t < 4) \otimes (1 < p_T^a < 2)$ GeV/c. Trigger-particle azimuthal angle relative to event planes $\phi_s = \phi^t - \Psi_2$ is selected out-of-plane (left) to in-plane (right). Centrality is 0%–10% (top) to 40%–50% (bottom).

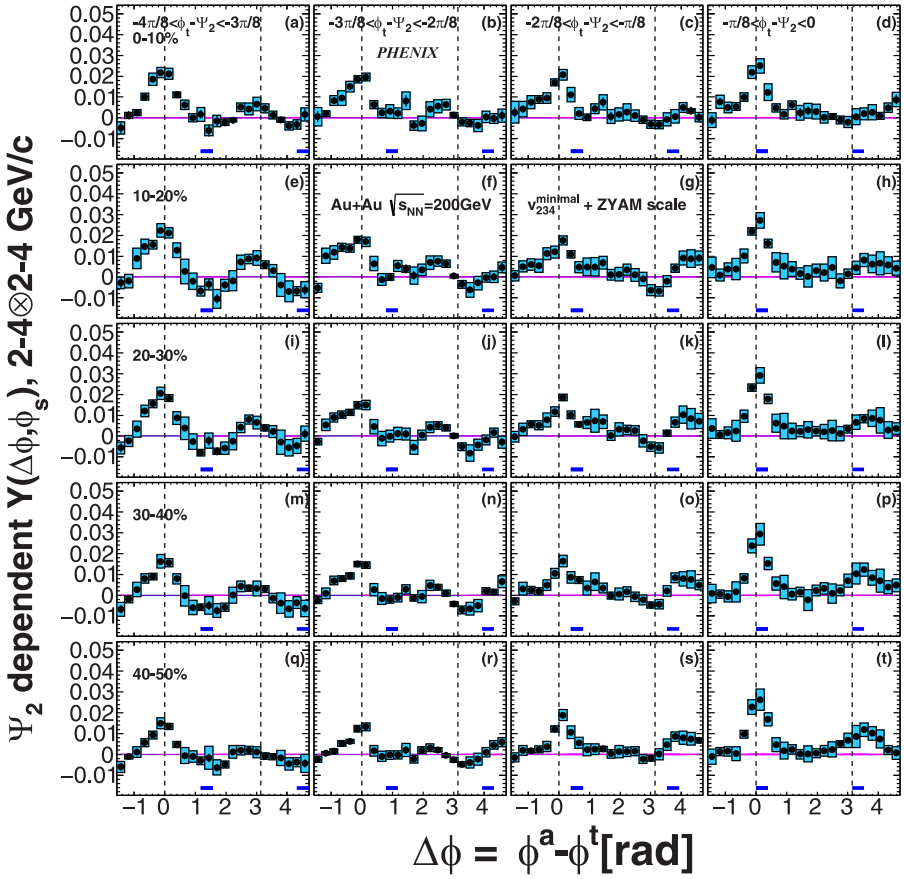

FIG. 30. Ψ_2-dependent per-trigger yields $Y(\Delta\phi, \phi_s)$ for $(2 < p_T^t < 4) \otimes (2 < p_T^a < 4)$ GeV/c. Trigger-particle azimuthal angle relative to event planes $\phi_s = \phi^t - \Psi_2$ is selected out-of-plane (left) to in-plane (right). Centrality is 0%–10% (top) to 40%–50% (bottom).

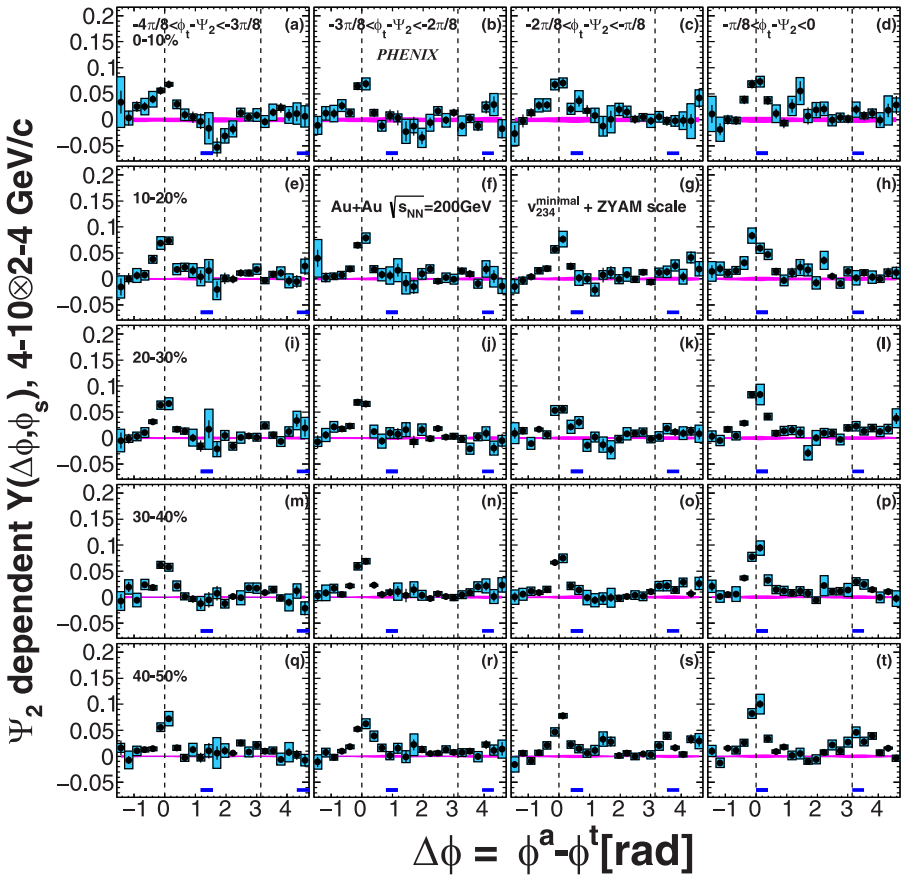

FIG. 31. Ψ_2-dependent per-trigger yields $Y(\Delta\phi, \phi_s)$ for $(4 < p_T^t < 10) \otimes (2 < p_T^a < 4)$ GeV/c. Trigger-particle azimuthal angle relative to event planes $\phi_s = \phi^t - \Psi_2$ is selected out-of-plane (left) to in-plane (right). Centrality is 0%–10% (top) to 40%–50% (bottom).

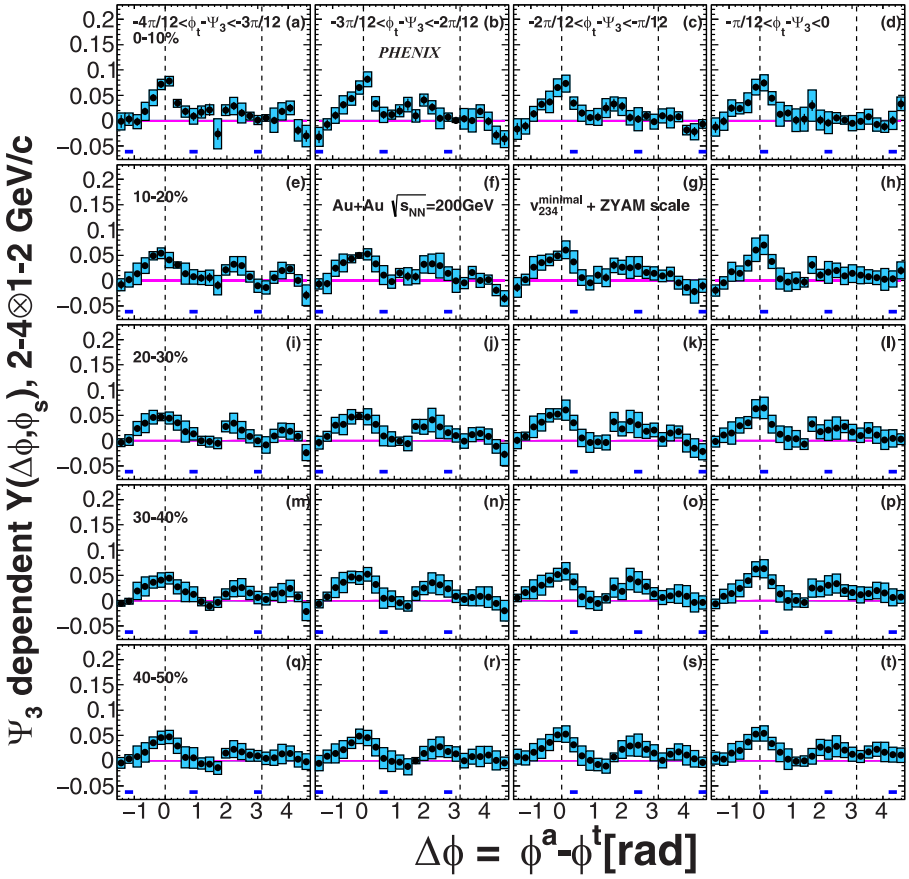

FIG. 32. Ψ_3-dependent per-trigger yields $Y(\Delta\phi, \phi_s)$ for $(2 < p_T^t < 4) \otimes (1 < p_T^a < 2)$ GeV/c. Trigger-particle azimuthal angle relative to event planes $\phi_s = \phi^t - \Psi_3$ is selected out-of-plane (left) to in-plane (right). Centrality is 0%–10% (top) to 40%–50% (bottom).

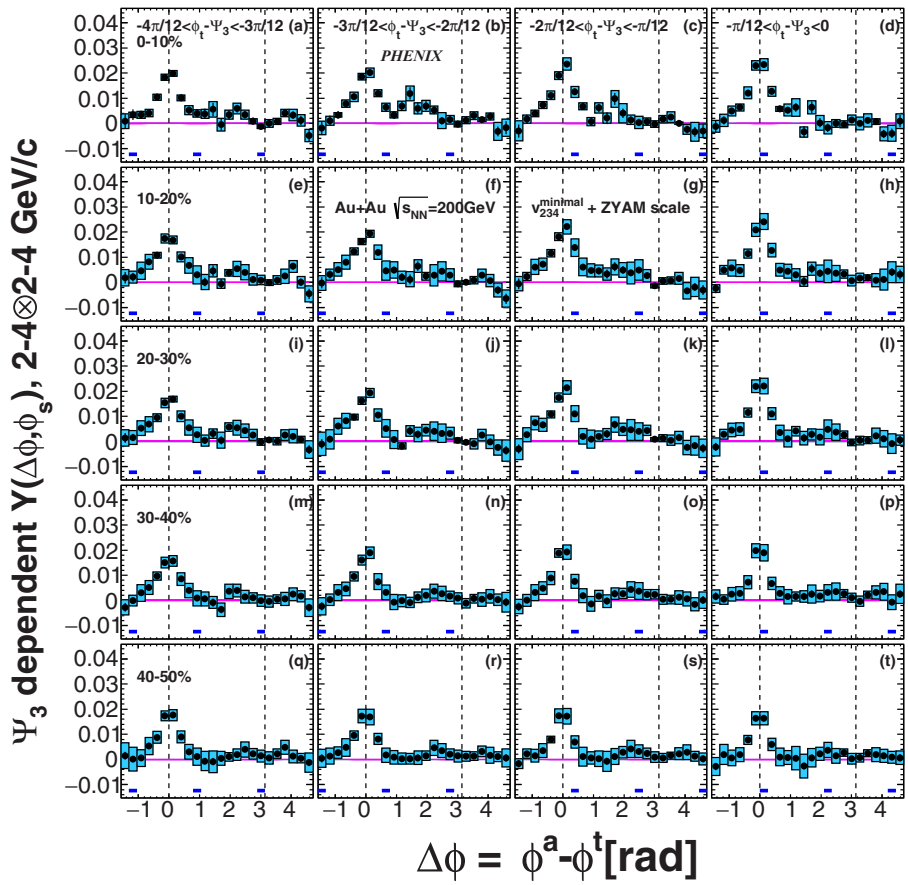

FIG. 33. Ψ_3-dependent per-trigger yields $Y(\Delta\phi, \phi_s)$ for $(2 < p_T^t < 4) \otimes (2 < p_T^a < 4)$ GeV/c. Trigger-particle azimuthal angle relative to event planes $\phi_s = \phi^t - \Psi_3$ is out-of-plane (left) to in-plane (right). Centrality is 0%–10% (top) to 40%–50% (bottom).

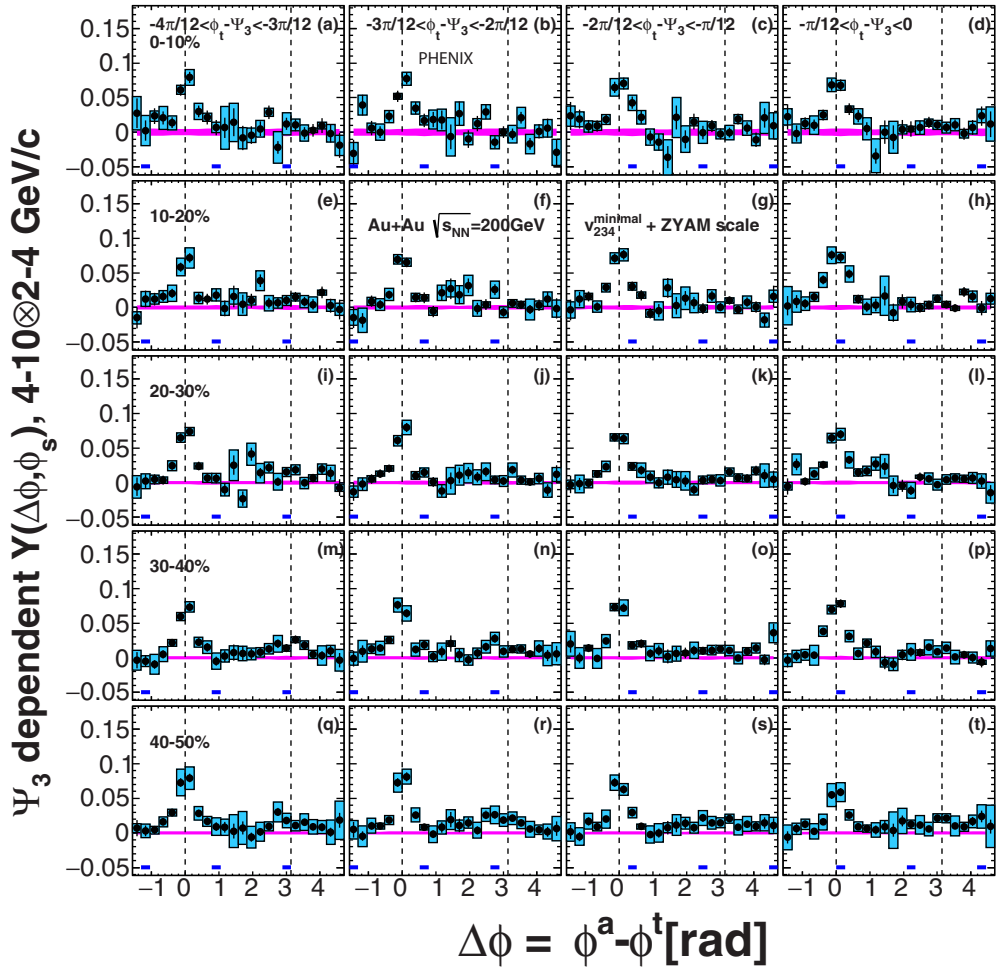

FIG. 34. Ψ_3-dependent per-trigger yields $Y(\Delta\phi, \phi_s)$ for $(4 < p_T^t < 10) \otimes (2 < p_T^a < 4)$ GeV/c. Trigger-particle azimuthal angle relative to event planes $\phi_s = \phi^t - \Psi_3$ is selected out of plane (left) to in-plane (right). Centrality is 0%–10% (left) to 40%–50% (right).

[1] X.-N. Wang and M. Gyulassy, Gluon Shadowing and Jet Quenching in $A + A$ Collisions at $\sqrt{s} = 200$ GeV, Phys. Rev. Lett. **68**, 1480 (1992).

[2] I. Arsene *et al.* (BRAHMS Collaboration), Quark gluon plasma and color glass condensate at RHIC? The Perspective from the BRAHMS experiment, Nucl. Phys. A **757**, 1 (2005).

[3] B. B. Back, M. D. Baker, M. Ballintijn, D. S. Barton, B. Becker *et al.*, The PHOBOS perspective on discoveries at RHIC, Nucl. Phys. A **757**, 28 (2005).

[4] J. Adams *et al.* (STAR Collaboration), Experimental and theoretical challenges in the search for the quark gluon plasma: The STAR Collaboration's critical assessment of the evidence from RHIC collisions, Nucl. Phys. A **757**, 102 (2005).

[5] K. Adcox *et al.* (PHENIX Collaboration), Formation of dense partonic matter in relativistic nucleus-nucleus collisions at RHIC: Experimental evaluation by the PHENIX Collaboration, Nucl. Phys. A **757**, 184 (2005).

[6] S. S. Adler *et al.* (PHENIX Collaboration), Suppressed π^0 Production at Large Transverse Momentum in Central Au + Au Collisions at $\sqrt{s_{NN}} = 200$ GeV, Phys. Rev. Lett. **91**, 072301 (2003).

[7] S. S. Adler *et al.* (PHENIX Collaboration), High-p_T charged hadron suppression in Au + Au collisions at $\sqrt{s_{NN}} = 200$ GeV, Phys. Rev. C **69**, 034910 (2004).

[8] J. Adams *et al.* (STAR Collaboration), Evidence from d + Au Measurements for Final State Suppression of High p_T Hadrons in Au + Au Collisions at RHIC, Phys. Rev. Lett. **91**, 072304 (2003).

[9] S. Chatrchyan *et al.* (CMS Collaboration), Study of high-p_T charged particle suppression in PbPb compared to pp collisions at $\sqrt{s_{NN}} = 2.76$ TeV, Eur. Phys. J. C **72**, 1945 (2012).

[10] G. Aad *et al.* (ATLAS Collaboration), Measurements of the Nuclear Modification Factor for Jets in Pb + Pb Collisions at $\sqrt{s_{NN}} = 2.76$ TeV with the ATLAS Detector, Phys. Rev. Lett. **114**, 072302 (2015).

[11] G. Aad *et al.* (ATLAS Collaboration), Measurement of the jet radius and transverse momentum dependence of inclusive jet suppression in lead-lead collisions at $\sqrt{s_{NN}} = 2.76$ TeV with the ATLAS detector, Phys. Lett. B **719**, 220 (2013).

[12] Jaroslav Adam *et al.* (ALICE Collaboration), Measurement of jet suppression in central Pb-Pb collisions at $\sqrt{s_{NN}} = 2.76$ TeV, Phys. Lett. B **746**, 1 (2015).

[13] T. Renk, Theoretical assessment of jet-hadron correlations, Phys. Rev. C **87**, 024905 (2013).

[14] G.-Y. Qin and X.-N. Wang, Jet quenching in high-energy heavy-ion collisions, Int. J. Mod. Phys. E **24**, 1530014 (2015).

[15] C. Adler *et al.* (STAR Collaboration), Disappearance of Back-to-Back High p_T Hadron Correlations in Central Au + Au Collisions at $\sqrt{s_{NN}} = 200$ GeV, Phys. Rev. Lett. **90**, 082302 (2003).

[16] A. Adare *et al.* (PHENIX Collaboration), Suppression of away-side jet fragments with respect to the reaction plane in Au + Au collisions at $\sqrt{s_{NN}} = 200$ GeV, Phys. Rev. C **84**, 024904 (2011).

[17] B. I. Abelev *et al.* (STAR Collaboration), Studying parton energy loss in heavy-ion collisions via direct-photon and charged-particle azimuthal correlations, Phys. Rev. C **82**, 034909 (2010).

[18] S. Chatrchyan *et al.* (CMS Collaboration), Studies of jet quenching using isolated-photon+jet correlations in PbPb and pp collisions at $\sqrt{s_{NN}} = 2.76$ TeV, Phys. Lett. B **718**, 773 (2013).

[19] L. Adamczyk *et al.* (STAR Collaboration), Jet-like correlations with direct-photon and neutral-pion triggers at $\sqrt{s_{NN}} = 200$ GeV, Phys. Lett. B **760**, 689 (2016).

[20] A. Adare *et al.* (PHENIX Collaboration), Medium Modification of Jet Fragmentation in Au + Au Collisions at $\sqrt{s_{NN}} = 200$ GeV Measured in Direct Photon-Hadron Correlations, Phys. Rev. Lett. **111**, 032301 (2013).

[21] G. Agakishiev *et al.* (STAR Collaboration), System size and energy dependence of near-side dihadron correlations, Phys. Rev. C **85**, 014903 (2012).

[22] C. Nattrass, N. Sharma, J. Mazer, M. Stuart, and A. Bejnood, Disappearance of the Mach cone in heavy-ion collisions, Phys. Rev. C **94**, 011901 (2016).

[23] L. Adamczyk *et al.* (STAR Collaboration), Jet-Hadron Correlations in $\sqrt{s_{NN}} = 200$ GeV $p + p$ and Central Au + Au Collisions, Phys. Rev. Lett. **112**, 122301 (2014).

[24] G. Aad *et al.* (ATLAS Collaboration), Measurement of inclusive jet charged-particle fragmentation functions in Pb + Pb collisions at $\sqrt{s_{NN}} = 2.76$ TeV with the ATLAS detector, Phys. Lett. B **739**, 320 (2014).

[25] S. Chatrchyan *et al.* (CMS Collaboration), Measurement of jet fragmentation in PbPb and pp collisions at $\sqrt{s_{NN}} = 2.76$ TeV, Phys. Rev. C **90**, 024908 (2014).

[26] V. Khachatryan *et al.* (CMS Collaboration), Correlations between jets and charged particles in PbPb and pp collisions at $\sqrt{s_{NN}} = 2.76$ TeV, J. High Energy Phys. 02 (2016) 156.

[27] K. Aamodt *et al.* (ALICE Collaboration), Particle-Yield Modification in Jet-Like Azimuthal Dihadron Correlations in Pb-Pb Collisions at $\sqrt{s_{NN}} = 2.76$ TeV, Phys. Rev. Lett. **108**, 092301 (2012).

[28] A. Adare *et al.* (PHENIX Collaboration), Trends in Yield and Azimuthal Shape Modification in Dihadron Correlations in Relativistic Heavy Ion Collisions, Phys. Rev. Lett. **104**, 252301 (2010).

[29] J. Adams *et al.* (STAR Collaboration), Direct Observation of Dijets in Central Au + Au Collisions at $\sqrt{s_{NN}} = 200$ GeV, Phys. Rev. Lett. **97**, 162301 (2006).

[30] B. I. Abelev *et al.* (STAR Collaboration), System size dependence of associated yields in hadron-triggered jets, Phys. Lett. B **683**, 123 (2010).

[31] H. Agakishiev *et al.* (STAR Collaboration), Studies of di-jet survival and surface emission bias in Au+Au collisions via angular correlations with respect to back-to-back leading hadrons, Phys. Rev. C **83**, 061901 (2011).

[32] B. Alver and G. Roland, Collision geometry fluctuations and triangular flow in heavy-ion collisions, Phys. Rev. C **81**, 054905 (2010).

[33] J. Xu and C. M. Ko, The effect of triangular flow on di-hadron azimuthal correlations in relativistic heavy ion collisions, Phys. Rev. C **83**, 021903 (2011).

[34] G. Aad *et al.* (ATLAS Collaboration), Measurement of the azimuthal anisotropy for charged particle production in $\sqrt{s_{NN}} = 2.76$ TeV lead-lead collisions with the ATLAS detector, Phys. Rev. C **86**, 014907 (2012).

[35] A. Adare *et al.* (PHENIX Collaboration), Measurements of Higher-Order Flow Harmonics in Au + Au Collisions at $\sqrt{s_{NN}} = 200$ GeV, Phys. Rev. Lett. **107**, 252301 (2011).

[36] K. Aamodt *et al.* (ALICE Collaboration), Higher Harmonic Anisotropic Flow Measurements of Charged Particles in Pb-Pb Collisions at $\sqrt{s_{NN}} = 2.76$ TeV, Phys. Rev. Lett. **107**, 032301 (2011).

[37] S. Chatrchyan *et al.* (CMS Collaboration), Measurement of higher-order harmonic azimuthal anisotropy in PbPb collisions at $\sqrt{s_{NN}} = 2.76$ TeV, Phys. Rev. C **89**, 044906 (2014).

[38] C. Shen, Z. Qiu, H. Song, J. Bernhard, S. Bass, and U. Heinz, The iEBE-VISHNU code package for relativistic heavy-ion collisions, Comput. Phys. Commun. **199**, 61 (2016).

[39] Z.-W. Lin, C. M. Ko, B.-A. Li, B. Zhang, and S. Pal, Multi-phase transport model for relativistic heavy ion collisions, Phys. Rev. C **72**, 064901 (2005).

[40] S. Voloshin and Y. Zhang, Flow study in relativistic nuclear collisions by Fourier expansion of azimuthal particle distributions, Z. Phys. C: Part. Fields **70**, 665 (1996).

[41] J.-Y. Ollitrault, Anisotropy as a signature of transverse collective flow, Phys. Rev. D **46**, 229 (1992).

[42] A. M. Poskanzer and S. A. Voloshin, Methods for analyzing anisotropic flow in relativistic nuclear collisions, Phys. Rev. C **58**, 1671 (1998).

[43] P. Sorensen, Implications of space-momentum correlations and geometric fluctuations in heavy-ion collisions, J. Phys. G **37**, 094011 (2010).

[44] S. S. Adler *et al.* (PHENIX Collaboration), Dense-Medium Modifications to Jet-Induced Hadron Pair Distributions in Au + Au Collisions at $\sqrt{s_{NN}} = 200$ GeV, Phys. Rev. Lett. **97**, 052301 (2006).

[45] B. I. Abelev *et al.* (STAR Collaboration), Long range rapidity correlations and jet production in high energy nuclear collisions, Phys. Rev. C **80**, 064912 (2009).

[46] A. Adare *et al.* (PHENIX Collaboration), Transverse momentum and centrality dependence of dihadron correlations in Au + Au collisions at $\sqrt{s_{NN}} = 200$ GeV: Jet-quenching and the response of partonic matter, Phys. Rev. C **77**, 011901 (2008).

[47] A. Adare *et al.* (PHENIX Collaboration), Dihadron azimuthal correlations in Au + Au collisions at $\sqrt{s_{NN}} = 200$ GeV, Phys. Rev. C **78**, 014901 (2008).

[48] A. Adare *et al.* (PHENIX Collaboration), System Size and Energy Dependence of Jet-Induced Hadron Pair Correlation Shapes in Cu + Cu and Au + Au Collisions at $\sqrt{s_{NN}} = 200$ and 62.4 GeV, Phys. Rev. Lett. **98**, 232302 (2007).

[49] H. Agakishiev *et al.* (STAR Collaboration), Event-plane-dependent dihadron correlations with harmonic v_n subtraction in Au + Au collisions at $\sqrt{s_{NN}} = 200$ GeV, Phys. Rev. C **89**, 041901 (2014).

[50] B. Alver *et al.* (PHOBOS Collaboration), High Transverse Momentum Triggered Correlations Over a Large Pseudorapidity Acceptance in Au + Au Collisions at $\sqrt{s_{NN}} = 200$ GeV, Phys. Rev. Lett. **104**, 062301 (2010).

[51] B. I. Abelev *et al.* (STAR Collaboration), Indications of Conical Emission of Charged Hadrons at RHIC, Phys. Rev. Lett. **102**, 052302 (2009).

[52] M. M. Aggarwal *et al.* (STAR Collaboration), Azimuthal dihadron correlations in d + Au and Au + Au collisions at $\sqrt{s_{NN}} = 200$ GeV from STAR, Phys. Rev. C **82**, 024912 (2010).

[53] S. Chatrchyan *et al.* (CMS Collaboration), Centrality dependence of dihadron correlations and azimuthal anisotropy harmonics in PbPb collisions at $\sqrt{s_{NN}} = 2.76$ TeV, Eur. Phys. J. C **72**, 2012 (2012).

[54] G. Aad *et al.* (ATLAS Collaboration), Measurement of the distributions of event-by-event flow harmonics in lead-lead collisions at $\sqrt{s_{NN}} = 2.76$ TeV with the ATLAS detector at the LHC, J. High Energy Phys. 11 (2013) 183.

[55] G. Aad *et al.* (ATLAS Collaboration), Measurement of the correlation between flow harmonics of different order in lead-lead collisions at $\sqrt{s_{NN}} = 2.76$ TeV with the ATLAS detector, Phys. Rev. C **92**, 034903 (2015).

[56] S. Acharya *et al.* (ALICE Collaboration), Systematic studies of correlations between different order flow harmonics in Pb-Pb collisions at $\sqrt{s_{NN}} = 2.76$ TeV, Phys. Rev. C **97**, 024906 (2018).

[57] V. Khachatryan *et al.* (CMS Collaboration), Evidence for transverse-momentum- and pseudorapidity-dependent event-plane fluctuations in PbPb and pPb collisions, Phys. Rev. C **92**, 034911 (2015).

[58] J. Adams *et al.* (STAR Collaboration), Azimuthal anisotropy in Au + Au collisions at $\sqrt{s_{NN}} = 200$ GeV, Phys. Rev. C **72**, 014904 (2005).

[59] B. B. Back *et al.* (PHOBOS Collaboration), Energy Dependence of Directed Flow Over a Wide Range of Pseudorapidity in Au + Au Collisions at RHIC, Phys. Rev. Lett. **97**, 012301 (2006).

[60] B. I. Abelev *et al.* (STAR Collaboration), System-Size Independence of Directed Flow at the Relativistic Heavy-Ion Collider, Phys. Rev. Lett. **101**, 252301 (2008).

[61] L. Adamczyk *et al.* (STAR Collaboration), Beam-Energy Dependence of the Directed Flow of Protons, Antiprotons, and Pions in Au + Au Collisions, Phys. Rev. Lett. **112**, 162301 (2014).

[62] B. Abelev *et al.* (ALICE Collaboration), Directed Flow of Charged Particles at Midrapidity Relative to the Spectator Plane in Pb-Pb Collisions at $\sqrt{s_{NN}} = 2.76$ TeV, Phys. Rev. Lett. **111**, 232302 (2013).

[63] C. Marquet and T. Renk, Jet quenching in the strongly-interacting quark-gluon plasma, Phys. Lett. B **685**, 270 (2010).

[64] S. Afanasiev *et al.* (PHENIX Collaboration), High-pT π^0 Production with Respect to the Reaction Plane in Au + Au Collisions at $\sqrt{s_{NN}} = 200$ GeV, Phys. Rev. C **80**, 054907 (2009).

[65] K. Adcox *et al.* (PHENIX Collaboration), PHENIX central arm tracking detectors, Nucl. Instrum. Methods Phys. Res., Sect. A **499**, 489 (2003).

[66] C. Adler, A. Denisov, E. Garcia, M. J. Murray, H. Strobele *et al.*, The RHIC zero degree calorimeter, Nucl. Instrum. Methods Phys. Res., Sect. A **470**, 488 (2001).

[67] E. Richardson *et al.* (PHENIX Collaboration), A reaction plane detector for PHENIX at RHIC, Nucl. Instrum. Methods Phys. Res., Sect. A **636**, 99 (2011).

[68] A. Adare *et al.* (PHENIX Collaboration), Deviation from quark-number scaling of the anisotropy parameter v_2 of pions, kaons, and protons in Au + Au collisions at $\sqrt{s_{NN}} = 200$ GeV, Phys. Rev. C **85**, 064914 (2012).

[69] S. S. Adler *et al.* (PHENIX Collaboration), Jet structure from dihadron correlations in d + Au collisions at $\sqrt{s_{NN}} = 200$ GeV, Phys. Rev. C **73**, 054903 (2006).

[70] J. Barrette *et al.* (E877 Collaboration), Proton and pion production relative to the reaction plane in Au + Au collisions at AGS energies, Phys. Rev. C **56**, 3254 (1997).

[71] N. N. Ajitanand, J. M. Alexander, P. Chung, W. G. Holzmann, M. Issah, R. A. Lacey, A. Shevel, A. Taranenko, and P. Danielewicz, Decomposition of harmonic and jet contributions to particle-pair correlations at ultra-relativistic energies, Phys. Rev. C **72**, 011902 (2005).

[72] J. Adams *et al.* (STAR Collaboration), Distributions of Charged Hadrons Associated with High Transverse Momentum Particles in pp and Au + Au Collisions at $\sqrt{s_{NN}} = 200$ GeV, Phys. Rev. Lett. **95**, 152301 (2005).

[73] J. Bielcikova, S. Esumi, K. Filimonov, S. Voloshin, and J. P. Wurm, Elliptic flow contribution to two particle correlations at different orientations to the reaction plane, Phys. Rev. C **69**, 021901 (2004).

[74] J.-Y. Ollitrault, Reconstructing azimuthal distributions in nucleus-nucleus collisions, arXiv:nucl-ex/9711003.

[75] L. Yan and J.-Y. Ollitrault, v_4, v_5, v_6, v_7: Nonlinear hydrodynamic response versus LHC data, Phys. Lett. B **744**, 82 (2015).

[76] G. Aad *et al.* (ATLAS Collaboration), Measurement of event-plane correlations in $\sqrt{s_{NN}} = 2.76$ TeV lead-lead collisions with the ATLAS detector, Phys. Rev. C **90**, 024905 (2014).

[77] G. D'Agostini, A multidimensional unfolding method based on Bayes' theorem, Nucl. Instrum. Methods Phys. Res., Sect. A **362**, 487 (1995).

[78] T. Adye, *Unfolding Algorithms and Tests using RooUnfold*, Proceedings of the PHYSTAT 2011 Workshop, CERN, Geneva, Switzerland, January 2011, CERN-2011-006, pp. 313–318.

[79] T. Sjostrand, S. Mrenna, and P. Z. Skands, PYTHIA 6.4 physics and manual, J. High Energy Phys. 05 (2006) 026.